JGR Solid Earth

RESEARCH ARTICLE
10.1029/2025JB031939

Multi-Observable Thermochemical Tomography: New Advances and Applications to the Superior and North Australian Cratons

I. Fomin[1], J. C. Afonso[2,3,4], A. Gorbatov[5], F. Salajegheh[1], R. Dave[6], F. A. Darbyshire[7], S. M. Hansen[8], B. Hejrani[5], M. W. Haynes[5], and K. Czarnota[5]

[1]School of Natural Sciences, Macquarie University, Sydney, NSW, Australia, [2]Faculty of Geo-Information and Earth Observation (ITC), University of Twente, Enschede, The Netherlands, [3]Department of Earth and Space Sciences, Southern University of Science and Technology Shenzhen, Guangdong, China, [4]School of Natural Sciences and CODES, University of Tasmania, Dynnyrne, TAS, Australia, [5]Geoscience Australia, Canberra, ACT, Australia, [6]Geological Survey of Canada, Vancouver, BC, Canada, [7]Centre de Recherche Geotop, Université du Québec à Montréal, Montréal, QC, Canada, [8]School of Engineering, Macquarie University, Sydney, NSW, Australia

Abstract Imaging the Earth's thermochemical structure is crucial for understanding its dynamics and evolution. Moreover, the increased demand for critical minerals and geothermal energy driven by the energy transition has intensified the need for reliable subsurface models. Multi-Observable Thermochemical Tomography (MTT) is a simulation-based, probabilistic inversion platform designed to harness the combined sensitivities of multiple geophysical data sets and thermodynamic modeling. It produces internally consistent estimates of the Earth's interior as probability distributions, offering a powerful means for uncertainty quantification. Here, we present an updated MTT formalism and assess its benefits and limitations to image the thermochemical structure of the lithosphere-asthenosphere system. Individual and combined sensitivities of different observables to parameters of interest (e.g., temperature, composition, crustal architecture) are explored using challenging synthetic models. Our findings demonstrate that a judicious combination of observables can retrieve complex thermochemical structures relevant to greenfields exploration. We then apply MTT to study two cratonic regions of geological and economic significance. In the Superior Craton, we jointly invert receiver functions, gravity anomalies, gravity gradients, geoid anomalies, Rayleigh-wave dispersion curves, absolute elevation and surface heat flow. In the North Australian Craton, we incorporate new data from the AusArray and add teleseismic P- and S-phase travel times to the data sets. The imaged lithospheric architectures provide new insights into the tectonic evolution of these two regions and the physical meaning of geophysical signatures. Additionally, these models offer unique proxies to guide exploration efforts for clean energy and critical minerals and serve as reference models for future high-resolution studies.

Plain Language Summary Imaging the Earth's interior is a fundamental goal of geophysics. As the need for critical minerals and geothermal energy grows to support the shift to cleaner energy sources, accurate information about the Earth's subsurface becomes even more important. In this context, Multi-Observable Thermochemical Tomography (MTT) is a powerful method that combines various types of land-based and satellite-derived data to create detailed images of the Earth's interior. We improved and used this method to study two regions of geological significance and with significant mineral endowment: the Superior Craton and the North Australian Craton. Our results show that MTT can accurately map complex structures underground, which is essential for finding resources. These models also help us understand the evolution of these regions and provide valuable information for guiding future studies and exploration.

Key Points:

- A new multi-algorithm implementation of Multi-observable Thermochemical Tomography (MTT) in spherical coordinates
- MTT can accurately retrieve thermochemical anomalies in the lithosphere relevant to energy and mineral exploration
- New thermochemical models of the Superior Craton and the North Australian Craton with unprecedented resolution

Supporting Information:

Supporting Information may be found in the online version of this article.

Correspondence to:

J. C. Afonso,
juan.afonso@utas.edu.au

Citation:

Fomin, I., Afonso, J. C., Gorbatov, A., Salajegheh, F., Dave, R., Darbyshire, F. A., et al. (2026). Multi-observable thermochemical tomography: New advances and applications to the superior and North Australian cratons. *Journal of Geophysical Research: Solid Earth*, *131*, e2025JB031939. https://doi.org/10.1029/2025JB031939

Received 19 MAY 2025
Accepted 24 NOV 2025

Author Contributions:

Conceptualization: J. C. Afonso, A. Gorbatov
Data curation: I. Fomin, B. Hejrani
Formal analysis: I. Fomin, J. C. Afonso, A. Gorbatov, F. A. Darbyshire, M. W. Haynes
Funding acquisition: J. C. Afonso, A. Gorbatov, M. W. Haynes, K. Czarnota
Methodology: I. Fomin, J. C. Afonso
Project administration: K. Czarnota
Resources: A. Gorbatov, R. Dave, B. Hejrani, M. W. Haynes
Software: I. Fomin, F. Salajegheh, S. M. Hansen
Supervision: J. C. Afonso, K. Czarnota
Validation: F. A. Darbyshire
Visualization: I. Fomin
Writing – original draft: I. Fomin, J. C. Afonso, A. Gorbatov, F. A. Darbyshire, M. W. Haynes

1. Introduction

Obtaining reliable estimates of the physical state of the Earth's interior (e.g., thermochemical structure, stress and strain distributions) constitutes a central goal of solid Earth geophysics and underpins evolutionary models of the Earth. The interest in this type of subsurface information, particularly at lithospheric scale, has recently grown considerably as a result of its relevance for supporting and resourcing the energy transition and related green technologies. For instance, exploring for deep, superhot rock geothermal energy, and critical minerals and strategic materials such as copper, lithium and Rare Earth Elements (REEs), requires detailed knowledge of the subsurface temperature structure and bulk lithologies across a range of scales (e.g., Haynes et al., 2020; Hoggard

Writing – review & editing: I. Fomin, J. C. Afonso, A. Gorbatov, F. A. Darbyshire, M. W. Haynes

et al., 2020; Kirkby et al., 2022; Skirrow et al., 2018). National initiatives like Geoscience Australia's Exploring for the Future program exemplify the significance of understanding a nation's subsurface in uncovering additional mineral resources and facilitating the transition to greener technologies (Czarnota et al., 2020).

Given this context, much effort has been invested in the past four decades, by academia and industry alike, in the development of sophisticated geophysical imaging techniques (e.g., Afonso, Moorkamp et al., 2016; Berkhout, 2014; Ismail-Zadeh et al., 2023; Tromp, 2020; Zhang et al., 2023). Seismic and electromagnetic methods are among the most powerful and widely used (e.g., Manassero et al., 2024; Moorkamp et al., 2016; Moorkamp, 2017; Rawlinson et al., 2014; Telford et al., 1990; Vozar et al., 2014; Zhang et al., 2023). However, although seismic velocities and/or electrical conductivity anomalies are useful proxies, they alone cannot constrain the thermochemical structure of the Earth's interior (e.g., Afonso, Moorkamp et al., 2016). Additionally, modern exploration frameworks need access to reliable measures of the uncertainties associated with every relevant model parameter (e.g., temperature, composition, density, seismic velocity) to reduce exploration risk, assist decision-making processes and guide future data acquisition programs. This type of global uncertainty quantification is typically computationally expensive and therefore uncommon in traditional applications dominated by deterministic inverse methods.

Multi-observable Thermochemical Tomography (MTT) is a novel Earth modeling approach specifically designed to image the physical state of the lithosphere and assess the full range of uncertainties (Afonso, Fullea, Griffin et al., 2013, Afonso, Fullea, Yang et al., 2013; Afonso, Rawlinson et al., 2016). MTT adopts a thermodynamically consistent approach to jointly invert multiple geophysical data sets with complementary sensitivities to the main fields of interest. The inverse problem is (well-) posed as a statistical inference problem and solved within a probabilistic framework that requires long Markov Chain Monte Carlo (MCMC) simulations (cf., Kaipio & Somersalo, 2005; Tarantola, 2005). Despite the many advantages of fully probabilistic approaches, as the dimension of the parameter space grows, it becomes increasingly difficult to locate and sample the regions of high probability to obtain representative estimates of the true posterior probability density function (i.e., the solution to the inverse problem). This so-called *curse of dimensionality* makes MTT computationally demanding. The computational cost arises from the need to solve forward problems millions of times.

Previous work highlighted the main advantages of MTT and showed that it is feasible for high-resolution regional studies with up to 10-20 $\times$ 10^3 free parameters with modest computational resources (e.g., Afonso, Rawlinson et al., 2016; Afonso et al., 2022). However, the number of key parameters in a continental-scale or global MTT study can easily exceed 10^6 and the solution of forward problems in 3D becomes significantly more involved. Here, we present a new conceptual and computational version of MTT in spherical coordinates based on a "multi-method" approach that combines (a) advanced MCMC algorithms to solve the ultra-high dimensional sampling problem, (b) efficient and scalable parallelization strategies for both the sampling problem and the forward solvers, and (c) reduced-order modeling techniques to accelerate the computation of difficult forward problems in MTT. Specifically, highly optimized MPI/OpenMP drivers and new solvers for body wave tomography, gravity potential and receiver functions allow for considerable speed up of the inversion compared to previous Cartesian implementations. First, we demonstrate the benefits and feasibility of our approach with a complex synthetic model designed to explore the reliability and applicability of the method for different geological settings. In particular, we show that relatively large MTT problems (≈50,000–100,000 parameters) are now practical even with limited computational resources. For even larger problems, the estimated computational cost remains well within the capabilities of typical computer clusters in many institutions around the world. Second, we apply the new approach to two different sets of data in the Superior Craton and the North Australian Craton. Both regions are well endowed in mineral resources, but they offer critical complementary information. While the Superior Craton has been extensively studied over decades of geophysical surveys, the North Australian Craton remains a frontier exploration area and the focus of recent high-quality data collection efforts. The Superior Craton then provides a well-documented baseline, while the North Australian Craton allows for the application of our techniques in a less explored territory, demonstrating their performance across diverse geological settings.

2. MTT: General Considerations

Multi-observable Thermochemical Tomography is a simulation-driven, joint inversion approach where multiple data sets with key complementary sensitivities are inverted to estimate the present-day physical state of the Earth's interior. MTT allows the space of valid solutions to be reduced and enhances our ability to obtain internally

consistent, multi-parameter models with greater explanatory power (i.e., they are consistent with a multitude of constraints/observations, Afonso, Fullea, Griffin et al. (2013), Afonso, Rawlinson et al. (2016)). The use of multiple observables with complementary sensitivities and resolutions is particularly important for distinguishing compositional and thermal anomalies in the lithosphere, which requires independent constraints on the bulk density and seismic velocity (mostly on S-waves, but independent information on P-wave speeds is also advantageous). This is best illustrated by the opposite effects that composition and temperature have on the density to shear-wave seismic velocity ratio (ρ/Vs) of peridotites (Afonso et al., 2010; Deschamps et al., 2002; Forte & Perry, 2000; Godey et al., 2004; Perry et al., 2003). More specifically, the above arguments are true in cases where information on seismic velocities comes from travel-time measurements or related observations. These include travel-time tomography, surface-wave tomography and finite-frequency tomography (the most common methods in seismic imaging). The use of full-waveform techniques (e.g., Fichtner et al., 2013), based on accurate numerical solutions of the wave equation, offer complementary sensitivity to both bulk density and seismic velocity (particularly impedance formulations) exploiting only one type of data (the full seismogram within the bandwidth of interest). This makes full-waveform methods a particularly attractive option for future MTT applications, especially those focusing on shallow structures.

The *primary* parameters inverted for in the MTT are the main thermodynamic variables, such as temperature, pressure and bulk composition, from which all other *secondary* parameters (e.g., shear modulus, bulk density) are consistently derived (Afonso, Fullea, Griffin et al., 2013, Afonso, Fullea, Yang et al., 2013). In MTT, all secondary physical parameters are linked to the primary thermodynamic parameters via a full thermodynamic model and an internally consistent thermodynamic database (e.g., Connolly, 2009; Stixrude & Lithgow-Bertelloni, 2011). Therefore, all secondary parameters are linked to each other in a thermodynamically consistent manner and they cannot vary in isolation from each other, while the uncertainties arising from the accuracy of thermodynamic parameters remain within 3%–4% for the seismic velocities and 2%–3% for the densities (e.g., Connolly & Khan, 2016), and fall within the standard deviations of recovered parameters, as we will demonstrate in this manuscript. This also means that the forward problems are coupled in a self-consistent manner (i.e., changing one parameter affects all other parameters and forward problems according to the thermodynamic formalism), thus guaranteeing that the results do not violate fundamental laws of thermodynamics (e.g., Maxwell's relationships); something that cannot be assured with the more common approach of using parameterized or empirical relations between density and seismic wave speed variations (see Afonso, Fullea, Griffin et al. (2013); Khan & Connolly (2008) for detailed discussions on uncertainties arising from thermodynamic formalisms). However, the price to pay for this attribute is that a large number of free-energy minimizations (numerical optimizations themselves) need to be performed during an inversion; typically between 10^8 and 10^{10} times. In practical applications, some of this computational burden can be alleviated by using semi-empirical relationships, surrogate/reduced order models or pre-computed tables of thermodynamic properties (e.g., Afonso et al., 2015; Kumar et al., 2020, 2022; Pilia et al., 2023; Zunino et al., 2011). In this work, we do not use such approximations and solve the full energy minimization problem on the fly for the entirety of the simulation/inversion.

2.1. Forward Problems

To date, the main forward problems that have been used in MTT studies (either in its 3D or 1D form) include the computation of (a) conductive lithospheric geotherms, (b) the system's Gibbs free-energy (via numerical optimization), (c) gravity potential, gravity anomalies and Marussi tensor, (d) surface-wave dispersion curves, (e) absolute elevation, (f) teleseismic travel-times (body-wave tomography), (g) synthetic seismograms for receiver functions (RFs), (h) the Stokes problem for instantaneous flow, and (i) the magnetotelluric impedance tensor. While the simultaneous solution of all these forward problems as part of a single inversion has not been attempted yet (due to data availability issues rather than computational ones), examples of joint inversions using large subsets can be found in Shan et al. (2014), Afonso, Rawlinson et al. (2016), Guo et al. (2016), Qashqai et al. (2016, 2018), Jones et al. (2017), A. Zhang et al. (2019, 2020), Yang et al. (2021), Afonso et al. (2022) and Manassero et al. (2024). In the present work, we will restrict ourselves to the first seven forward problems for both synthetic and real world scenarios. Importantly, with the exception of Afonso et al. (2022), all previous MTT studies were set up in Cartesian coordinates; a limitation that we remove in the current implementation in spherical coordinates.

2.2. The Inverse Problem

The inverse problem is posed as a statistical inference problem according to a Bayesian formulation (cf. Afonso, Fullea, Griffin et al., 2013, Afonso, Fullea, Yang et al., 2013; Kaipio & Somersalo, 2005; Tarantola, 2005) and solved by Markov chain Monte Carlo (MCMC) algorithms (see below). From the conceptual point of view, the main question to be answered becomes what do we know about a certain parameter m? Rather than what is the actual value of m? From a computational point of view, this approach does not require (at least in principle) linearization of the physics involved and offers a natural and powerful platform for uncertainty quantification (e.g., Afonso, Fullea, Griffin et al., 2013, Afonso, Fullea, Yang et al., 2013; Dosso & Wilmut, 2006; Kaipio & Somersalo, 2005; Malinverno & Parker, 2006; Tarantola, 2005; Tarantola & Valette, 1981). Importantly, this probabilistic formulation is also a more amenable and general platform for combining realistic forward problems of diverse nature than matrix-based deterministic methods.

The existing knowledge about parameter m before considering data is encoded into a probability density function (PDF) known as the *prior* PDF. Bayes' theorem then provides the means to update our prior knowledge by making use of the available data via a *likelihood* function (i.e., a measure of how well the proposed model explains the data). The result of this update of our state of knowledge is another PDF over the parameter space referred to as the *posterior* PDF, which represents the most general solution to the inverse problem. Formally, we can write

$$\sigma(\mathbf{m}) \propto \mathcal{L}(\mathbf{m})\rho(\mathbf{m}) \tag{1}$$

where $\sigma(\mathbf{m})$ is the posterior PDF, $\rho(\mathbf{m})$ the prior PDF of the model parameters and $\mathcal{L}(\mathbf{m})$ the likelihood function. For simplicity of presentation, we assume independent Gaussian error statistics for each data set i, which allows us to write the likelihood function as

$$\mathcal{L}(m)_i = \frac{1}{2\pi\sigma_i^{N_i/2}} \exp\left[-\frac{\left(d_i^o - d_i^p\right)^2}{2\sigma_i^2}\right] \tag{2}$$

for all data types i = (elevation, geoid height, RFs, etc.), where σ_i is the data set uncertainty, N is the number of observations, d^o is the observed data and d^p is the predicted data (Afonso, Fullea, Griffin et al., 2013; Sambridge & Mosegaard, 2002; Tarantola, 2005; Wirth et al., 2016). If σ_i is considered known, we can write

$$\mathcal{L}(m)_i \propto \exp\left[-\varphi(m)_i\right] \tag{3}$$

where we introduce the misfit or error function

$$\varphi(m)_i = -\frac{\left(d_i^o - d_i^p\right)^2}{2\sigma_i^2} \tag{4}$$

A delicate topic when inverting multiple data sets ($i = 1,\ldots, k$) with different numbers of observations and/or poorly known uncertainties is how to balance their contribution to the overall misfit function or likelihood,

$$\mathcal{L}(m) = \prod_{i=1}^{i=k} w_i \mathcal{L}(m)_i \tag{5}$$

where w_i are weights that control the contribution of each partial likelihood to the overall likelihood. As mentioned above, here we assume that we can have reliable information on the observational uncertainties for all data sets and estimates of the weights assigned to each data set. In practice, we obtain "optimal" weights for each partial likelihood through experimentation with synthetic tests (see next section). We note, however, that hierarchical formulations (e.g., Bodin et al., 2012; Malinverno & Briggs, 2004) to allow for the automatic weighting of the data sets are straightforward to implement at the modest cost of increasing the parameter space and computational effort.

Posterior distributions (Equation 1) arising from complex physical problems are typically non-Gaussian and analytically intractable. In these cases, stochastic sampling methods offer the only practical approach for obtaining representative estimates of the posterior. Of these, MCMC methods are the most widely used and, to date, the most general. These methods are designed to generate Markov chains that have $\sigma(\mathbf{m})$ as their invariant or equilibrium density (Brooks et al., 2011; Kaipio & Somersalo, 2005). To do so, the algorithm produces piece-wise samples of $\sigma(\mathbf{m})$ in an iterative fashion by solving Equation 1 for a specific m at each iteration. When the algorithm is iterated a large number of times, the distribution of generated samples approximates $\sigma(\mathbf{m})$.

3. MTT in Practice: A Multi-Algorithm Approach

The need for efficient sampling of increasingly more complex distributions (e.g., narrow, multiple local minima) in high-dimensional spaces is reflected in the large number of MCMC algorithms that have been proposed in the past 15–20 years. However, as a rule of thumb, the more efficient an algorithm is, the more restricted its area of applicability (cf. Wolpert & Macready, 1997). Considering the ultra-high-dimensional spaces that characterize MTT of large-scale models, the complexities of the prior and posterior PDFs, the large number of forward problems that need to be solved, their strong nonlinearities and their overall computational complexity, there is no single algorithm that can efficiently solve the sampling (i.e., inverse) problem. To tackle these issues, we assemble multiple MCMC strategies in order to combine the strengths of different MCMC algorithms into a single inversion strategy (i.e., a multi-method approach in the sense of, e.g., Vrugt & Robinson (2007)). The implementation relies on an efficient and scalable parallelization of both MCMC chains and the forward problems. In particular, we want to combine complementary algorithms that can create an efficient and general computational environment to tackle MTT problems.

LitMod3D_4INV is the numerical platform of MTT and is developed around the Metropolis-Hastings acceptance criterion with a Cascade Rejection Rule (Mosegaard & Tarantola, 1995). When the data sets are independent, Cascade Metropolis increases computational efficiency by avoiding the computation of the most expensive forward problems if the proposed model is rejected based on inexpensive forward problems. We also adopt the Adaptive Metropolis (AM) strategy of Haario et al. (2001) to improve sampling efficiency and avoid pre-simulation tuning of the proposal distributions and associated performance issues. AM improves mixing and sampling efficiency by performing automatic and regular updates of the proposal covariance matrix during the simulation based on the history of the chain (cf. Haario et al., 2001; Spencer, 2021).

We further improve the sampling strategy by implementing the Multiple-Try Metropolis (MTM) and the Multiple-Try Metropolis Independent Sampler (MTMIS) (Liu, 1996; Liu et al., 2000). These allow us to utilize multiple computational cores to simultaneously compute multiple proposals and thus increase the efficiency of the sampling of the parameter space. We also make use of the Orthogonal MCMC (Martino et al., 2016) and Parallel Tempering (PT; Sambridge, 2013) algorithms to obtain an efficient combination of global exploration and local sampling of the most demanding problems. Importantly, the *LitMod3D_4INV* code allows the use of these algorithms individually or in various combinations according to the nature of the inverted data sets and the size of the numerical domain (see Section 6).

Besides accelerating the sampling itself, another way of improving the efficiency of MCMC simulations is by making the forward solvers faster. In *LitMod3D_4INV*, we use multiple Reduced Order modeling (ROM) techniques and individual parallelization to solve some of the most demanding forward problems. We refer the reader to Ortega-Gelabert et al. (2020) and Manassero et al. (2021) for details on these techniques. Other forward problems, like the potential field solver and the body-wave ray tracer, have been optimized using OpenMP and vectorization techniques to speed up the computations by a factor of 3–10 from their original implementations (Figures S3-10–S3-12 in Supporing Information S1). Furthermore, *LitMod3D_4INV* assigns individual chains (e.g., during PT runs) to independent CPUs, and subsequently distributes the proposal generation streams (MTM, MTMIS) between the available computational cores (using specific MPI libraries and data transfer optimizations proposed by Martino & Louzada (1997) and Li et al. (2009); Figure S3-12 in Supporing Information S1).

While Afonso, Rawlinson et al. (2016) adopted the Fast Marching Method of Rawlinson & Sambridge (2005) to compute seismic wave travel times, here we use an improved version of the ray tracing algorithm of Gorbatov et al. (2000, 2001), based on the pseudo-bending method of Koketsu & Sekine (1998). The main reason for this choice is increased efficiency in the computation of travel times in large models. Comparisons between predictions from the Fast Marching Method and our ray tracing approach are shown in Figures 7–9, in Text S3 of

Supporting Information S1. The RF approach was adopted from Ligorria & Ammon (1999) and based on the forward modeling developed by Randall (1994).

4. Model Discretization and Parameterization

The main parameterization and discretization scheme remains similar to that described in detail in Afonso, Fullea, Yang et al. (2013), Afonso, Rawlinson et al. (2016). Therefore, we only provide a brief summary here.

A *LitMod3D_4INV* model includes a region of the Earth extending from the surface down to the depth of 410 km (deeper domains are also straightforward to implement). The spatial discretization uses a set of spherical rectangular prisms (i.e., tesseroids) with typical lateral dimensions ranging from 0.25 to 2° in latitude/longitude. Each column has flexibility to include an arbitrary number of crustal layers. When semi-empirical relationships (e.g., Birch's Law) are used, each crustal layer is characterized by its thickness, radioactive heat production (RHP), Vp/Vs ratio, and bulk density (e.g., Afonso, Rawlinson et al., 2016). Other thermophysical parameters (e.g., bulk modulus, thermal expansion) are assumed constant. In contrast, free-energy minimization is always used for the mantle component, and all its physical parameters are derived consistently from the computed equilibrium assemblage (Afonso, Fullea, Yang et al., 2013; Connolly, 2009). Different mantle layers are allowed, each defined by its thickness and its major-element composition (e.g., SiO_2, Al_2O_3, FeO, MgO, CaO; Afonso, Fullea, Griffin et al., 2013, Afonso, Rawlinson et al., 2016). The depth to the lithosphere-asthenosphere boundary (LAB) is an important free parameter that separates the conduction-dominated from the convection-dominated domains. Once sampled, temperatures within the lithosphere are given by the solution of the heat conduction equation (Afonso, Fullea, Griffin et al., 2013, Afonso, Fullea, Yang et al., 2013). In the sublithospheric mantle, multiple temperature nodes are defined; their depths and temperatures are considered free parameters during the inversion (i.e., sampled at each iteration).

With these considerations, a typical realization of a model includes the following parameters for all columns: LAB depth, crustal thickness, density, Vp/Vs and RHP of each crustal layer, thickness and major-element composition of each mantle layer, temperature and depth of all sublithospheric nodes. Additional parameters associated with specific data sets can also be included. For instance, scaling factors for the amplitude of RFs and for the velocity jump at the crust-mantle interface can also be considered as unknowns and added to the vector of model parameters (see Section 6.2.1).

Once a valid proposal is generated and the thermal and compositional structures are sampled, the free-energy minimization problem is solved for all the relevant parts of the model (Figure 1). Since pressure depends on the density of the overlying material, which in turn depends on the P-T-C conditions, pressure is computed iteratively, as explained in Afonso, Fullea, Yang et al. (2013). The equilibrium assemblage and its thermophysical properties for all thermodynamic nodes at each iteration are computed with components of the software *Perple_X* (Connolly, 2009).

5. Numerical Examples and Performance Analysis

In this section, we illustrate the general features and performance of our method using a challenging synthetic model. The latter includes a number of geological/tectonic settings with abrupt horizontal and vertical discontinuities (Figures 2 and 3; Table 1) and a complex thermochemical structure.

5.1. Synthetic Model Setup

The model includes a low-topography continental background, a deep oceanic basin, and five high-elevation regions (e.g., mountain ranges) isostatically compensated by different contributions from the crust and lithospheric mantle (Table 1; Figures 2 and 3). The crust is made up of three layers (upper, middle and lower crust) with distinct densities, thicknesses, and Vp/Vs ratios. The mantle includes the lithospheric and the sublithospheric domains, each with a specific major-element composition. Both the lithospheric and sublithospheric domains have marked compositional anomalies. The sublithospheric mantle has additional temperature anomalies of different sizes and amplitudes, extending over multiple tectonic settings (Figure 3). This model represents a significant challenge to any inversion algorithm attempting to recover the physical state of the model.

The numerical domain extends for 50° longitude × 50° latitude, with its southern boundary located at 0° latitude. To minimize the so-called "inversion crime" (e.g., Kaipio & Somersalo, 2005), we compute all synthetic data sets

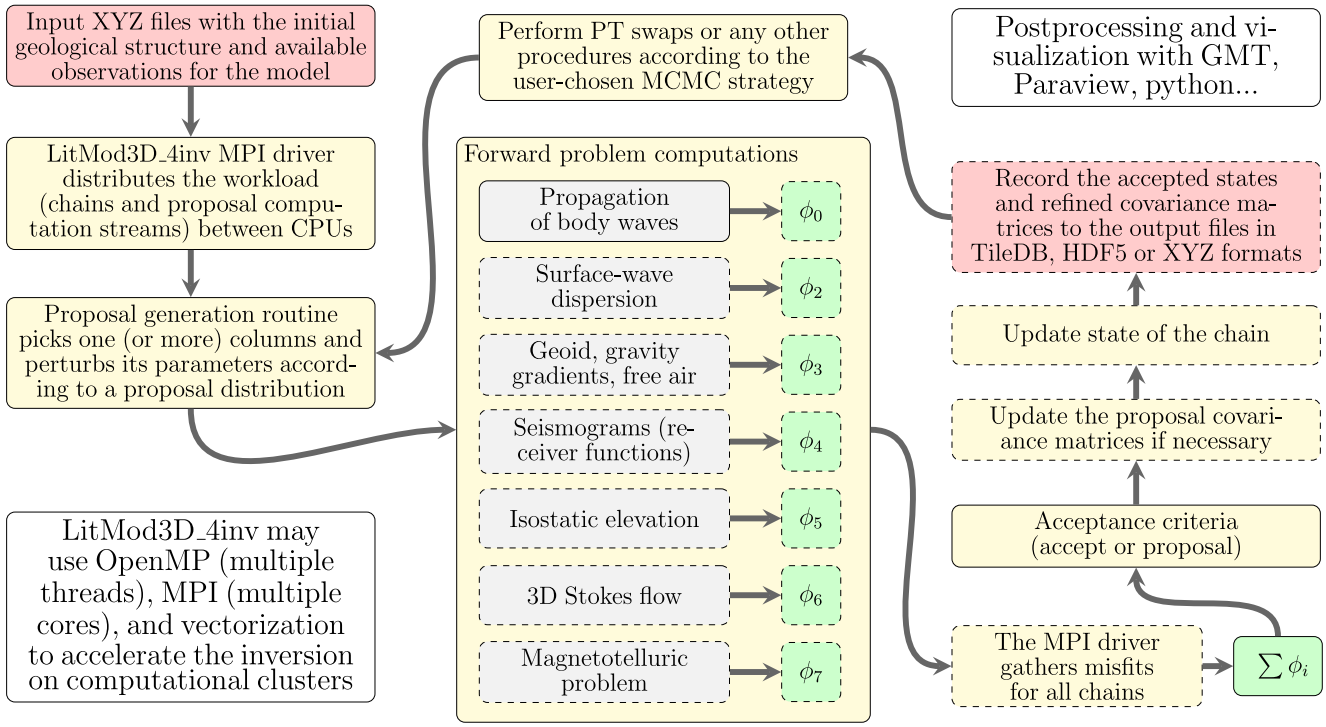

Figure 1. Computational workflow of *LitMod3D_4INV*. The sampler generates proposals for randomly chosen columns and the forward problems are solved. Multiple algorithms are combined to improve the efficiency of the sampling.

for a model with a surface discretization of 0.5° × 0.5° (i.e., 10,000 tesseroids), while during the inversion we use a surface discretization of 1° × 1° (i.e., 2,500 tesseroids; Figures 2 and 4). A total of 2,291 regularly spaced synthetic seismic stations were placed on the surface above sea level (Figure 2). Gaussian noise within realistic bounds was added to all synthetic observables.

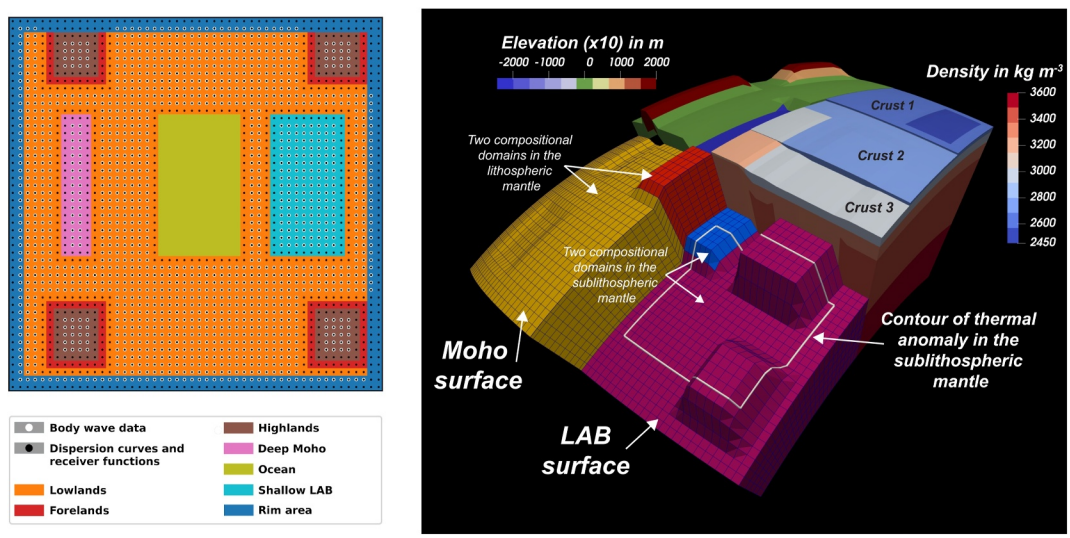

Figure 2. Left: Plan view of the main domains of the synthetic model described in Section 5.1 (see also Table 1). The blue rim around the model shows the regions that are omitted from the computation of misfits. Right: 3D rendering of the synthetic model highlighting the complexity of vertical and horizontal structures. Mantle compositional and thermal anomalies are indicated.

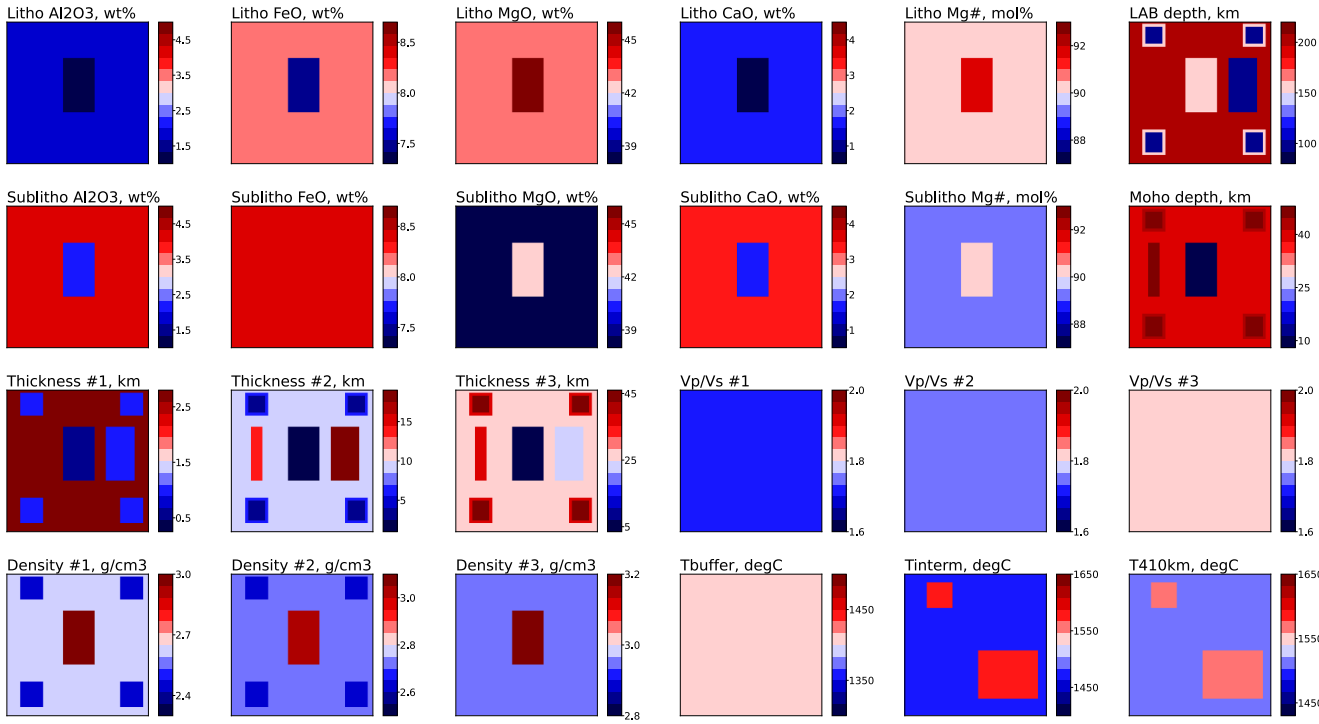

Figure 3. Maps showing the main thermochemical structure and anomalies of the synthetic model of Section 5.1. The terms "Litho" and "Sublitho" refer to the lithospheric and sublithospheric mantle, respectively. Thickness, Vp/Vs and density of the three crustal layers are shown in the third and fourth rows. The fourth row also contains the thermal anomalies ("Tinterm" and "T410 km") in the sublithospheric mantle.

The total number of unknowns in the model is $2500 \times (3 \times 3 + 4 \times 2 + 1) = 45{,}000$. Although still modest for a continental-scale model, the dimensionality of our synthetic model is representative of regional-scale studies. It is also significantly higher than those in most probabilistic geophysical inversions, and yet, small enough to permit us to run multiple inversions and tests with modest computational resources (see below).

5.2. Inversion Setup

We ran multiple independent inversions using different combinations of input data sets to assess the quality and reliability of the retrieved structure as a function of the type of input data. All simulations were run using the MTM algorithm on only 6 cores (with 6 independent proposals computed at each MCMC step). All simulations begin with a laterally homogeneous (i.e., layered) model and were run for no less than 17,000,000 iterations and no more than 25,000,000. We used uniform distributions as priors for all model parameters, except for mantle composition, which follows the sampling strategy of Afonso, Fullea, Griffin et al. (2013), Afonso, Rawlinson et al. (2016), based on correlations among oxides. In order to minimize prior biases in the parameter space, we used wide, yet realistic, ranges for all model parameters (Table 1). Specifically, the ranges for crustal layer thicknesses and LAB depth were set to ±50% of their original value. We allowed a ±10% range for crustal density and 1.6–2.0 for the Vp/Vs ratio of all crustal layers. For mantle composition, we allowed Al_2O_3, FeO, MgO and CaO contents to vary between 0.5 and 5.0 wt.%, 6.0 and 9.2 wt.%, 32.0 and 55.0 wt.% and 0.1 and 5.5 wt.%, respectively (SiO_2 is constrained by the content of the other oxides to satisfy $SiO_2 = 100 - (Al_2O_3 + FeO + MgO + CaO)$). These ranges encompass most of the natural variability observed in mantle xenoliths (Afonso, Fullea, Griffin et al., 2013). The temperature range for the sublithospheric thermal nodes was set to 1,300–1,650°C.

5.3. Results

Due to the difficulty in visualizing and interpreting ultra-high dimensional posterior distributions, here we adopt a common and pragmatic approach: we summarize the inversion results using the posterior means and standard deviations for each parameter of interest. Despite its simplicity, this approach is justified in the majority of the study region, as demonstrated in Text S6 of Supporting Information S1. Figure 5 shows the recovered structure by

Table 1
Properties of the Synthetic Model

Region				Background	Sea	Moho Ridge	LAB Ridge	Foreland	Tableland	Thermal anomaly	Proposal bounds	Initial guess
Latitude (at centers of columns)				10°…59°	28°…45°	28°…45°	28°…45°	50°…57° 50°…57° 13°…21° 13°…21°	51°…56° 51°…56° 14°…20° 14°…20°	48°…55° 16°…31°	–	–
Longitude (at centers of columns)				−15°…34°	5°…14°	−8°…−5°	19°…28°	−10°…−3° 24°…31° −10°…−3° 24°…31°	−9°…−4° 25°…30° −9°…−4° 25°…30°	−7°…0° 11°…30°	–	–
Elevation, km				0.1	−2.45	2	2	1	2	–	–	–
LAB depth, km				200	150	200	100	150	100	–	±50%	160
Crustal layers	Density	kg/m^3	1	2,600	3,000	2,600	2,600	2,450	2,450	2,600	±20%	–
			2	2,700	3,000	2,700	2,700	2,650	2,650	2,700	±20%	–
			3	2,950	3,200	2,950	2,950	2,950	2,950	2,800	±20%	–
	V_p/V_s	–	1	1.7	–	–	–	–	–	–	1.6..2.0	1.75
			2	1.75	–	–	–	–	–	–	1.6..2.0	1.75
			3	1.8	–	–	–	–	–	–	1.6..2.0	1.75
	Thickness	km	1	2.6	0.5	2.6	1	1	1	–	±50%	2.0
			2	9.63	1.47	13.06	17.91	5.97	3.17	–	±50%	10.0
			3	25.50	4.03	33.80	21.65	36.35	45.0	–	±50%	25.0
Mantle, wt.%	above LAB	SiO_2		45.60	45.15	45.60	45.60	45.60	45.60	–	–	45.97
		Al_2O_3		1.90	1.00	1.90	1.90	1.90	1.90	–	–	3.00
		FeO		8.13	7.50	8.13	8.13	8.13	8.13	–	–	8.34
		MgO		42.81	45.61	42.81	42.81	42.81	42.81	–	–	40.14
		CaO		1.56	0.74	1.56	1.56	1.56	1.56	–	–	2.55
	below LAB	SiO_2		45.72	45.67	45.72	45.72	45.72	45.72	–	–	45.97
		Al_2O_3		4.00	2.00	4.00	4.00	4.00	4.00	–	–	3.00
		FeO		8.39	8.36	8.39	8.39	8.39	8.39	–	–	8.34
		MgO		38.43	42.53	38.43	38.43	38.43	38.43	–	–	40.14
		CaO		3.46	1.65	3.46	3.46	3.46	3.46	–	–	2.55
T, °C	LAB + 40 km			1,410	1,410	1,410	1,410	1,410	1,410	1,410	1,300..1500	1,400
	Intermediate			1,470	1,470	1,470	1,470	1,470	1,470	1,570	1,400..1650	1,525
	410 km			1,510	1,510	1,510	1,510	1,510	1,510	1,560	1,430..1650	1,540

Note. If an anomaly overlaps with any other anomaly, the rightmost entry applies. SiO_2 content is computed as 100 minus the sum of the other four oxides.

a joint inversion of absolute elevation, Rayleigh wave phase velocity (periods 6–190 s), geoid anomaly, gravity gradients (diagonal components only), free-air gravity anomalies and P-wave and S-wave travel times (for phases S, Sn, P, Pn). Figure 4 shows a 3D rendering of the recovered thermal structure together with examples of computed teleseismic P and local Pn ray paths. Corresponding fits for some of the observation data sets are summarized in Figure 6. Despite the high complexity of the synthetic model, the inversion recovered all main structures and anomalies with considerable accuracy. In particular, the LAB and Moho depths are recovered within 2% of their true values for the majority of columns. The most uncertain features are the temperature anomalies in the sublithospheric mantle. This is not surprising given the lower sensitivity of the data sets to deep anomalies (Afonso, Fullea, Griffin et al., 2013). However, in real-world scenarios, increasing the period range of the dispersion data and/or including overtone information can increase the overall sensitivity to such anomalies.

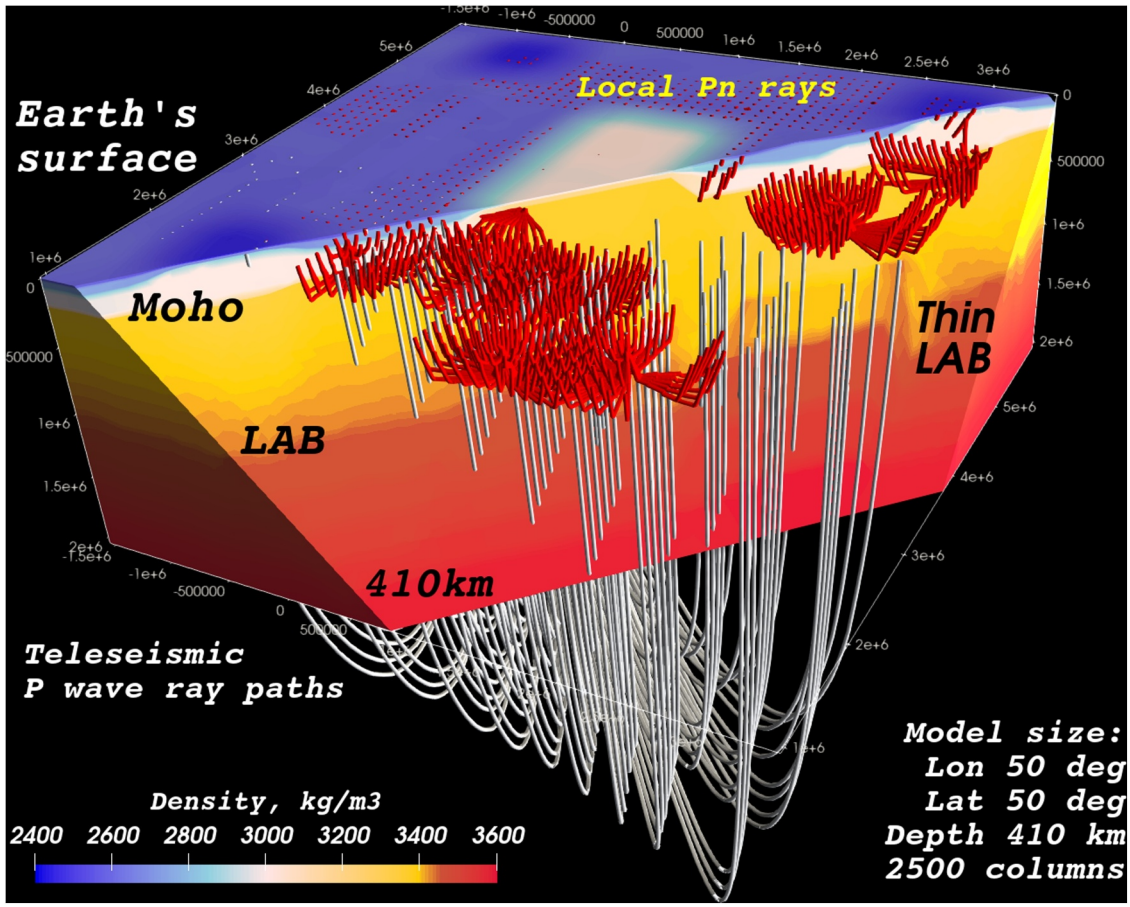

Figure 4. 3D rendering of the recovered synthetic model (plotted using Cartesian geometry) showing some of the body-wave ray paths computed during the inversion. Paths of P-waves from a teleseismic event are shown in white; local Pn phases are shown in red. A total of 100,000 ray paths were used as data in the inversion.

Considering the many inherent difficulties in identifying deep compositional anomalies from geophysical data, the accuracy of the retrieved results in Figure 5 is encouraging. However, there are clear biases in some fields. For instance, the Vp/Vs ratios of the first and second crustal layers are not well constrained. This is to be expected given the low sensitivity of the inverted data to this parameter. The inclusion of RFs results in more accurate estimates, particularly for the second crustal layer (see below). There is also a clear trade-off in some of the oxides. The Al_2O_3 and CaO contents in the lithosphere are slightly overestimated, while those of FeO and MgO are slightly underestimated. The reason for this trade-off is multi-fold, but the two main factors are (a) that Al_2O_3 and CaO contents control the amount of high-density, seismically fast phases in the system (e.g., garnet, clinopyroxene) and (b) the fact that the average original content of Al_2O_3 is close to its lower bound. Regarding the former factor, any excess in Al_2O_3 and/or CaO can be offset by a decrease in FeO content (and/or to a minor extent MgO content) without considerably affecting the physical properties of the aggregate (see also Afonso, Moorkamp et al. (2016) for further discussions on intrinsic trade-offs in the compositional space). The latter factor tends to result in asymmetric, long-tailed posterior PDFs for Al_2O_3, which in turn shifts the average or mean to slightly higher values.

Results from a systematic analysis of the effects of using different data sets in the inversion are shown in 1 and 2. Some general conclusions can be drawn from these experiments. First, the largest discrepancy between predicted and true values is observed in runs that invert: (a) elevation only, (b) elevation and P-to-S RFs and/or (c) elevation and body-wave travel times (Figures S1-1–S1-14 in Supporing Information S1). Second, the importance of the combined role/sensitivity of surface waves, geoid and gravity gradients in retrieving acceptable estimates of the full thermochemical structure is evident (models "k", and "m" in Figures S1-2–S1-14 or S2-1–S2-7 of Supporing Information S1). This observation is consistent with results from previous studies (Afonso et al., 2010; Afonso,

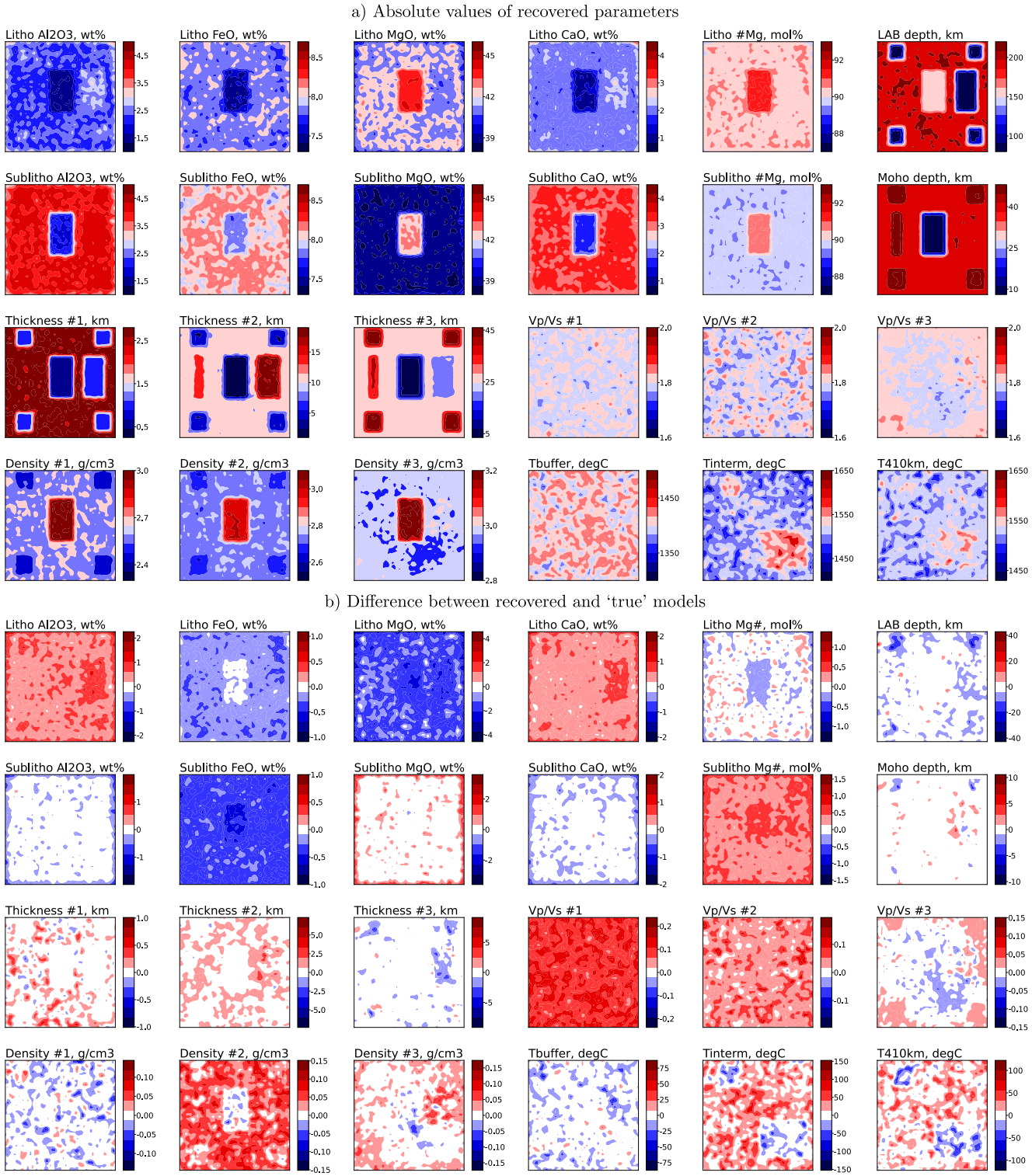

Figure 5. Summary of results from an inversion of synthetic data (elevation, geoid anomaly, free-air anomaly, gravity gradients, Rayleigh wave phase velocities and P and S body waves. (a) Absolute recovered values. Compare with "true" solution in Figure 3. (b) Absolute difference between recovered and "true" models (i.e., predicted minus "rue" values). As expected from the input data, the Vp/Vs values in the upper crust are poorly constrained; the recovered mean values cluster around the center of the proposal bounds.

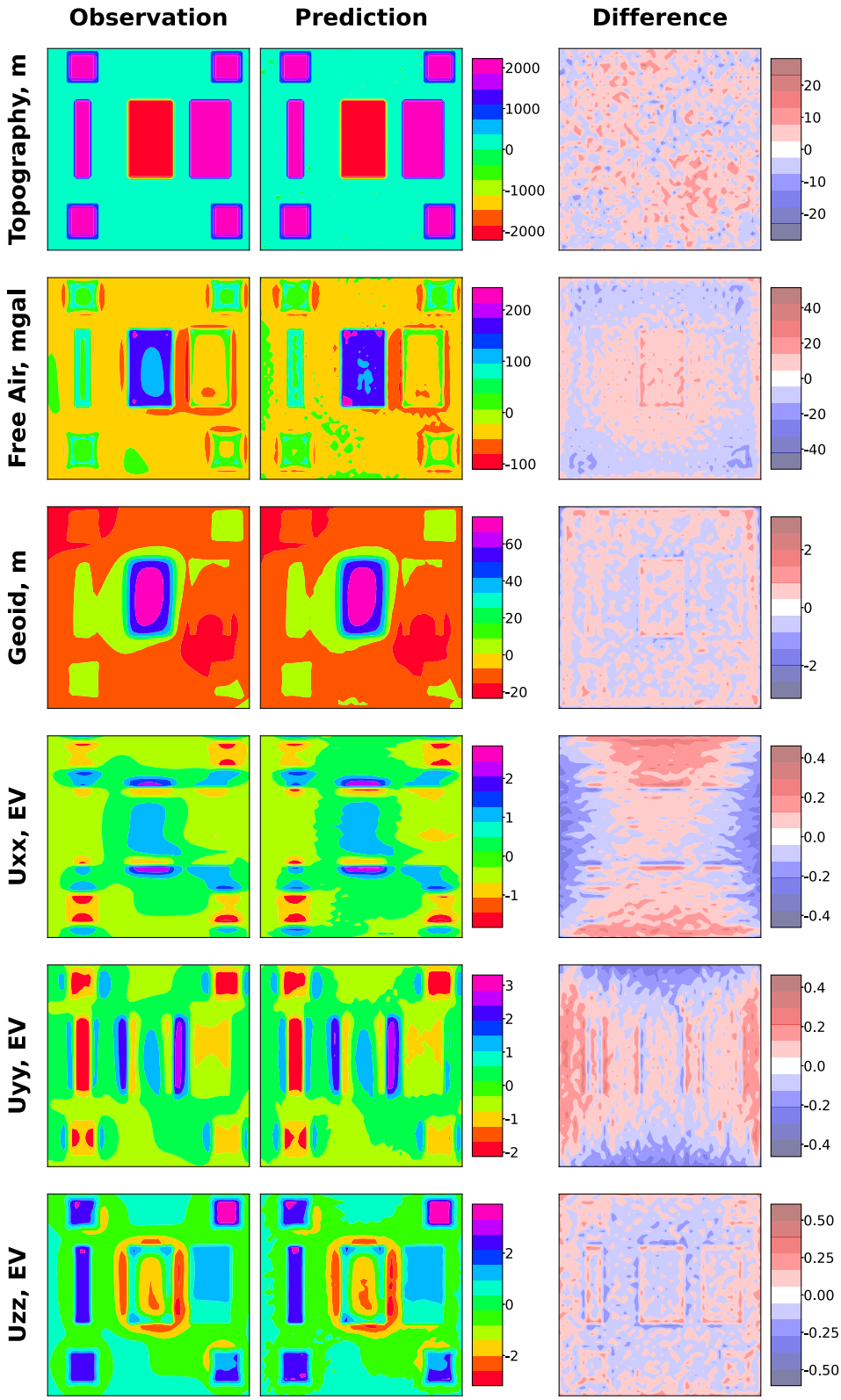

Figure 6. A joint inversion for absolute elevation, Rayleigh-wave phase velocity (periods 6–190 s), geoid anomaly, gravity gradients (diagonal components only), free-air gravity anomalies and P-wave and S-wave travel times (for S, Sn, P, Pn first arrivals) produced feasible fits for the supplied potential field data sets and Rayleigh-wave phase velocities (m/sec) at different periods. The predictions are compared against a synthetic data set with doubled spatial resolution.

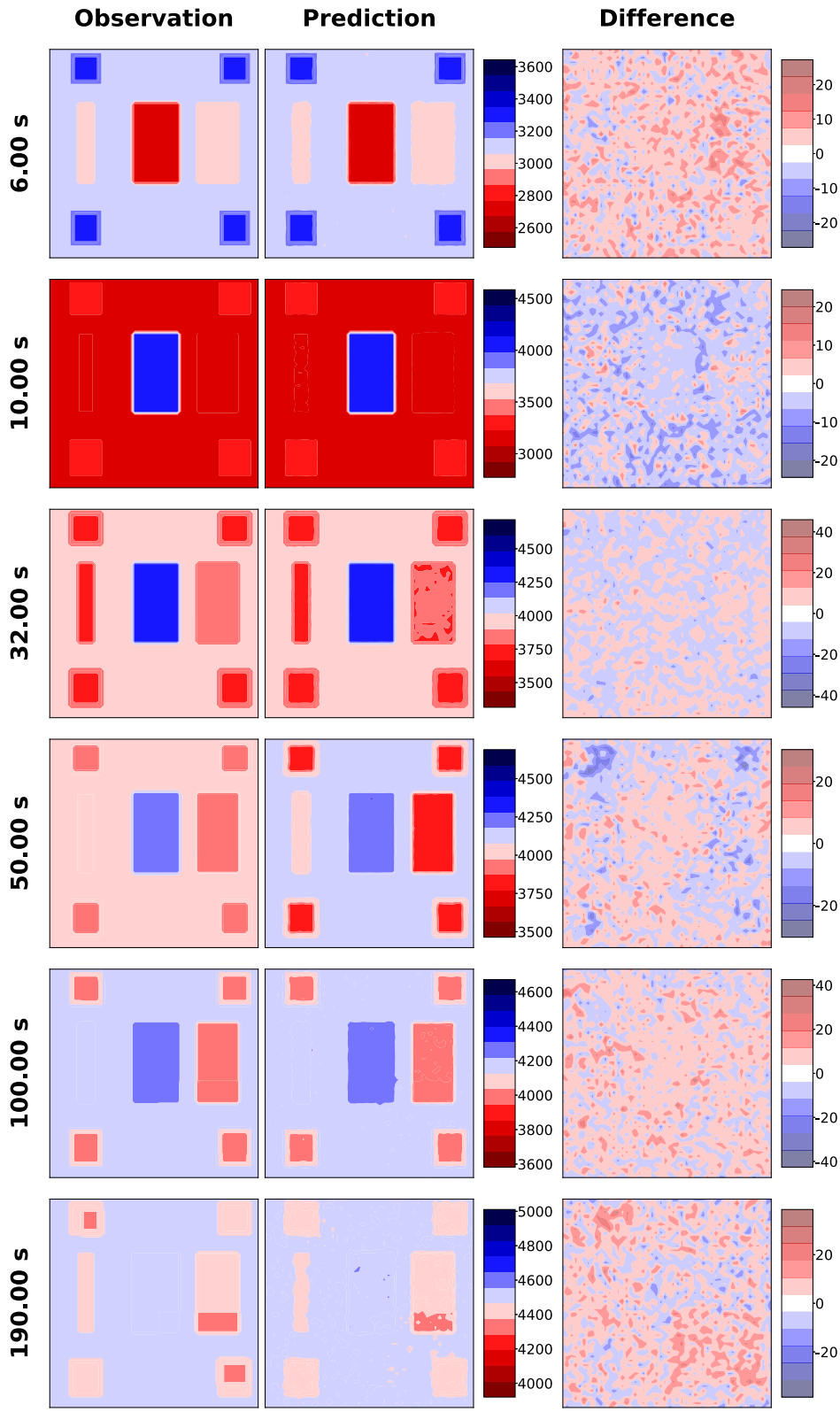

Figure 6. (Continued)

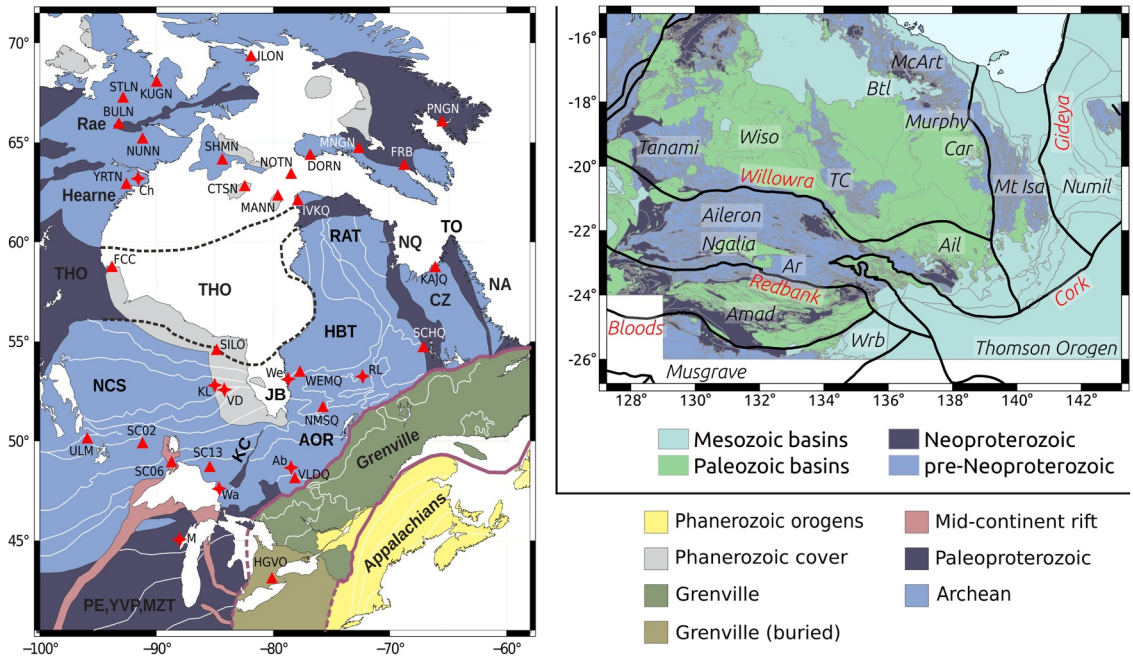

Figure 7. Left plot. Tectonic map of the eastern Canadian shield and its surroundings, modified from Hoffman (1988), Whitmeyer & Karlstrom (2007), St-Onge et al. (2009), Corrigan et al. (2009), Clowes (2010), Percival et al. (2012), Stein et al. (2014) and Rivers (2015). Abbreviations: THO, Trans-Hudson Orogen; PE,YVP, MZT, Penokean, Yavapai, Mazatzal belts; NQ, New Quebec Orogen; CZ, Core Zone; TO, Torngat Orogen; NA, Nain craton; KC, Kapuskasing complex; AOR, Abitibi-Opatica region; NCS, North Caribou Superterrane; HBT, Bienville/Hudson Bay Terrane; RAT, Rivière Arnaud Terrane; JB, James Bay. White lines denote domain and subprovince boundaries. Red triangles with alphanumeric codes denote seismograph stations for which RF analysis was carried out. Red stars mark locations of kimberlites with mantle xenocrysts which were used for comparison with the inversion results. Abbreviations: VD, Victor (Smit et al., 2014; Stachel et al., 2017) and Delta (Smit et al., 2014) areas; We, Wemindji (Zurevinski & Mitchell, 2011); Me, Menominee (Xu et al., 2020); RL, Renard (Hunt et al., 2012) and Lynx (Van Rythoven et al., 2011); Wa, Wawa (Kaminsky et al., 2002; Stachel et al., 2006); Ch, Churchill (Zurevinski et al., 2008); KL, Kyle Lake (Attawapiskat area) (Sage, 2000); Ab, Abitibi (Lawley et al., 2018). Right plot. The bedrock geology (without Cenozoic cover) of the Australian study area following data of Stewart et al. (2020) and Korsch & Doublier (2015), including Northern Territory, western Queensland, eastern Western Australia and northern South Australia. The major units include the Proterozoic Tanami block, the Tennant Creek inlier (TC), the Mount Isa inlier, the Arunta block (Ar), and the younger Aileron province. Major basins include the Paleozoic Amadeus (Amad) and Ngalia basin, McArthur (McArt), Warburton (Wrb) basins and the Mesozoic Beetaloo (Btl) and Carrara (Car) sub-basins. The study area is surrounded by the Phanerozoic Numil tectonic province and Thomson orogen, and Proterozoic Musgrave province. The major tectonic features of the area include the Redbank thrust zone and the Gideya suture zone, as well as the Willowra lineament and the Bloods Deformed Zone.

Fullea, Yang et al., 2013; Afonso, Rawlinson et al., 2016) and illustrates the combined sensitivity of bulk density and Vs in distinguishing temperature from compositional anomalies in the mantle (e.g., Afonso et al., 2010; Deschamps et al., 2002; Forte & Mitrovica, 2001; Forte & Perry, 2000; Karato & Karki, 2001; Perry et al., 2003; Simmons et al., 2009; Trampert et al., 2004). This is particularly important for deep compositional anomalies (Figure S2-S21 in Supporing Information S1). Third, the inclusion of P-to-S RFs improves the results in the crust substantially (models "e" and "l" in Figures S1-6 and S1-13 of Supporing Information S1), which in turn contributes to retrieving slightly better results in other model parameters (e.g., LAB depth, sublithospheric temperatures). The reason for this is clear; by reducing the range of acceptable models in the crust, compensatory trade-offs between crustal structure and other model parameters are also reduced. Fourth, contrary to a common belief, absolute FeO content is a difficult compositional parameter to constrain independently, at least in the upper mantle. However, the magnesium number Mg# and Al_2O_3 remain good and well-recovered proxies (see also Afonso, Fullea, Griffin et al. (2013), Afonso, Fullea, Yang et al. (2013)); lithospheric anomalies of the order of 1% in Mg# are clearly identifiable.

6. Applications to Real Data

We now apply our inversion method to two different input data sets in two different regions: (a) the Superior Craton and environs (Canada and the northern USA; Figures 7a) and (b) the North Australian Craton (Figure 7b). The data vector in the Superior Craton region comprises gravity anomalies, diagonal components of the Marussi tensor (gravity gradients), geoid anomalies, Rayleigh-wave dispersion curves (20–220 s), P-wave RFs, absolute

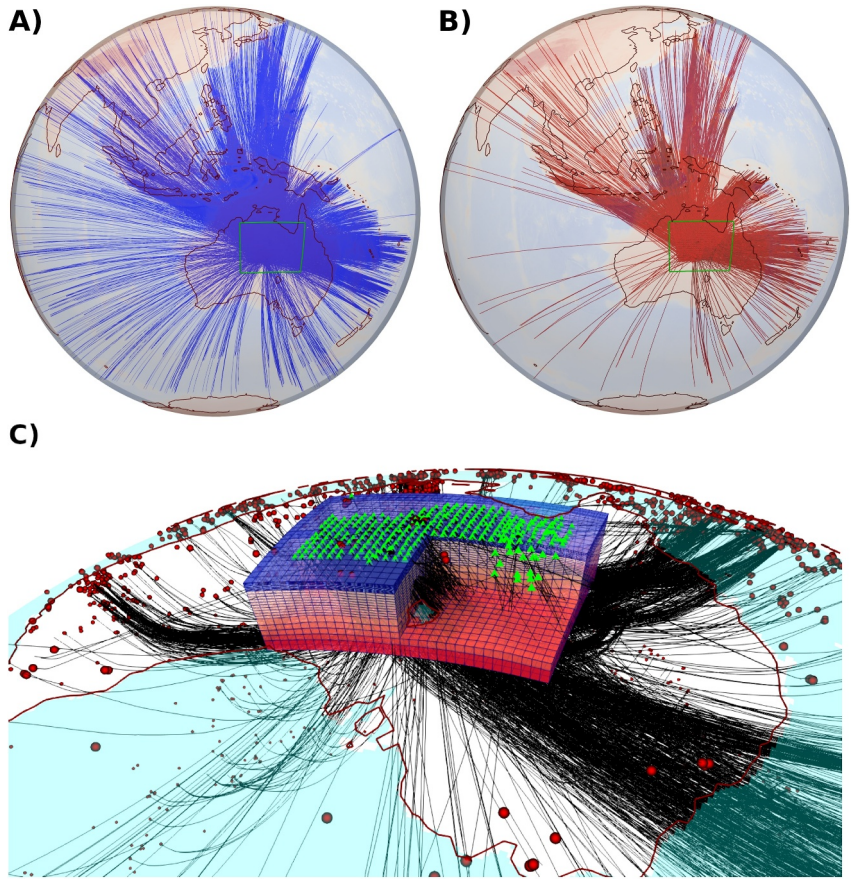

Figure 8. (a, b) P-wave ($N = 7{,}664$, blue lines) and S-wave ($N = 2{,}169$, red lines) ray paths used in our inversion. The green box indicates the extent of our numerical domain. (c) A 3D rendering of our North Australian Craton model embedded in a larger domain showing seismic rays used in our study. Red circles mark earthquake locations (for both P and S body waves) and green triangles denote the AusArray deployment. The grid shows the model discretization with the crust and mantle shown in bluish and reddish colors, respectively. The change in vertical spacing in the mantle corresponds to the LAB (with higher resolution in the lithospheric mantle). Note that the surface of the numerical box is placed on the surface of the map; the depth extension is "inside" the map.

elevation and surface heat flow. In the North Australian craton region, the data vector includes gravity anomalies, diagonal components of the gravity gradient, geoid anomalies, shorter period Rayleigh-wave dispersion curves (2.5–60 s), P-wave RFs, absolute elevation and teleseismic P- and S-phase travel times. The combined sensitivity of the data sets to deep vs shallow structure, the spatial distribution and frequency contents of seismic data, and the overall noise contaminating the two different data vectors are substantially different. Consequently, they present distinct yet complementary and illustrative challenges for our inversion scheme. Our focus will be on the imaging/detection of lithospheric structure rather than detailed tectonic/genetic interpretations.

6.1. Geological Background

6.1.1. The Superior Craton

The Superior Craton spans an area of 1.6 million km^2 across central and eastern Canada and the north-central USA (e.g., Thurston, 1991). It was assembled from several terranes with ages from ∼3 to 2.6 Ga, including metasedimentary belts, volcanic and plutonic belts and high-grade metamorphic domains (e.g., Percival et al., 2012). In the western and central Superior, terranes are oriented approximately east–west, whereas in the northeast, terrane orientation shifts to north–south. While some terranes, notably in the core of the Western Superior, have a continental provenance, others are considered to have oceanic, island-arc or continental margin characteristics, providing a unique record of tectonic evolution in the Archean. Assembly of the Superior Craton was complete by ∼2.6 Ga ago (e.g., Percival et al., 2006).

To the north and west of the Superior Craton, the Archean Rae and Hearne domains make up the composite Western Churchill Craton. The terminal collision between the two cratons in the Paleoproterozoic gave rise to the Trans-Hudson Orogen (THO), a structure that stretches across the central USA, central and northern Canada and into southern Greenland (e.g., Hoffman, 1988; St-Onge et al., 2006). In northern Canada, Phanerozoic sedimentary cover, including the intracratonic Hudson Bay Basin, conceals much of the THO, though its boundaries are visible in potential-field maps (e.g., Eaton & Darbyshire, 2010). In the east, further Paleoproterozoic orogenesis brought together the Archean Core Zone and North Atlantic craton, welded by the New Quebec and Torngat orogens (e.g., Corrigan et al., 2018).

South of the Superior Craton, Paleo- and Mesoproterozoic orogenesis added material to the growing Laurentian continent via a series of terrane accretions including the Penokean, Yavapai and Mazatzal domains (Whitmeyer & Karlstrom, 2007). The final stages in the assembly and evolution of the Precambrian Laurentian continent included rifting and extensive magmatism ~1.1 Ga ago which created the (failed) Keweenawan Mid-continent rift (e.g., Stein et al., 2015). Multi-stage orogenesis on the southeast margin of the Superior Craton created the Grenville province between ~1.2 and ~0.98 Ga ago (e.g., Rivers, 2015), associated with the assembly of the Rodinia supercontinent.

The breakup of Rodinia led to the opening, and subsequent closure, of the Iapetus ocean in the Paleozoic, forming the Appalachian mountain belt via a series of arc and continental collisions (e.g., Van Staal et al., 2012). This event completed the assembly of the eastern side of what is now the North American continent. From ~190 to ~100 Ma, parts of the Rae domain, THO, central Superior, southern Grenville and northern Appalachians were affected by magmatism that may be associated with interaction between the Great Meteor hotspot and the North American lithosphere (e.g., Heaman & Kjarsgaard, 2000; Sleep, 1990).

6.1.2. The North Australian Craton

The poorly exposed North Australian Craton spans an area of 1.5 million km^2 across central and northern Australia (e.g., Myers et al., 1996). It is characterized by predominantly Paleoproterozoic (1,870–1,800 Ma) metasedimentary and igneous rocks of several orogens and basins, including the Aileron (northern Arunta), Tennant Creek, Tanami, Murphy, McArthur and Mount Isa regions shown in Figure 7. Sparse outcrops and widespread isotopic evidence reveal that these Paleoproterozoic rocks are underlain by Neoarchean to Paleoproterozoic continental crust (e.g., Kumwenda et al., 2023). Most of the craton was assembled by 1.87–1.84 Ga, marked by the presence of thick sedimentary packages deformed and intruded by magmatic rocks with similar geochemical characteristics (Ahmad & Scrimgeour, 2013; Kumwenda et al., 2023).

The southern edge of the North Australian Craton is bounded by the east–west Central Australian Suture, separating it from the younger Paleoproterozoic to Mesoproterozoic (1,690–1,600 Ma) metasedimentary and metaigneous rocks of the Warumpi Province, accreted onto the craton around 1,640 Ma (Scrimgeour, 2015). Further to the south lies the Mesoproterozoic Musgrave Province with long-lived magmatism and sedimentation (1,600–1,060 Ma).

Over 70% of the North Australian Craton and its margins are overlain by Neoproterozoic to Mesozoic sedimentary basins. Neoproterozoic to Paleozoic basins of the Centralian Superbasin, such as the Amadeus, Ngalia and Georgina (and the Paleozoic Wiso Basin in the west) can reach thicknesses of up to ~8 km in local depocenters. These basins preserve flood basalts of the ~510 Ma Kalkarindji large igneous province (Glass & Phillips, 2006; Walter et al., 1995) and record intraplate deformation from the 600–530 Ma Peterman Orogeny and the 400–300 Ma Alice Springs Orogeny (Hand & Sandiford, 1999). During the Mesozoic, widespread shallow seas covered the east and north of the North Australian Craton, resulting in sedimentary sequences tens to hundreds of meters thick. Mesozoic subsidence and uplift are attributed to dynamic topography, largely related to subduction slab dynamics (Braz et al., 2021; Czarnota et al., 2014).

Geological mapping reveals notable differences in deformation styles, metamorphism, and structural trends across the North Australian Craton, but major boundaries and the nature of underlying lithospheric blocks remain hard to identify (Kumwenda et al., 2023). As a result, geophysical data are increasingly relied upon. Recent geophysical studies revealed variations in observed crustal and lithospheric thickness across the North Australian Craton of more than 30 and 150 km, respectively (Hoggard et al., 2020; Kennett et al., 2023). There is a growing consensus that this imaged architecture has been stable for several hundred million years, and likely >1 billion

years. In the southern portion of the craton (Figure 7), extreme gravity anomalies (~150 mGal) are attributed to displacements of the Moho developed during the Alice Springs Orogeny. Furthermore, regions of the thickest lithosphere and crust, located near the Murphy Inlier, appear to have been stable for over a billion years, as they control both the distribution of old sedimentary basins and continued mineral deposition (Czarnota et al., 2020a; Hoggard et al., 2020; Kennett et al., 2023).

The North Australian Craton is known for its mineral endowment, hosting world-class deposits of zinc, lead, silver, copper, and various critical minerals (Huston et al., 2021). Recent studies have highlighted connections between trans-lithospheric features, geodynamic setting, lithospheric mantle composition and the distribution of these deposits (e.g., Gibson et al., 2016; Hoggard et al., 2020; Huston et al., 2023). It is therefore crucial to the future of exploration programs to be able to synthesize data with sensitivity to the thermochemical structure of the lithosphere into reliable subsurface models.

6.2. Inversion Set Up: Initial Model, Parameterization and Prior Bounds

6.2.1. Superior Craton Region

The initial model for the inversion was taken from the results of a previous multi-observable probabilistic inversion using the *LitMod*1*D*_4*INV* software (Dave et al., 2024). This pseudo-3D model was based on a series of 1D inversions on a series of non-overlapping columns in a 1° tessellated grid. It consists of three crustal layers and three mantle layers. The latter include two subcontinental lithospheric mantle (SCLM) layers and the sublithospheric mantle. The two SCLM layers are separated by a mid-lithospheric discontinuity (MLD). The data sets used in Dave et al. (2024) were chosen to provide sensitivity to the SCLM structure, but the crustal component and structures in the uppermost 50 km were poorly constrained. Here we build on this initial model and focus on the crustal structure and the shallowest portion of the upper mantle. To achieve this, we made two important improvements. First, we increased the horizontal resolution to 0.5° × 1° (61 × 41 cells, compared to 1° × 2° in Dave et al. (2024)), which corresponds to column dimensions of ~55.7 km × 54 km to ~55.7 km × 84 km, depending on latitude. Second, we added three new input data sets with additional sensitivity to the shallow structure, namely gravity anomalies, gravity gradients and P-wave RF data (see below and Figure 7).

To maximize the information content from the RFs and achieve better fits to the waveforms, we also introduce three new features to our model with respect to that of Dave et al. (2024). The first one is an additional crustal layer (i.e., to give a 4-layer crustal model). The second is a gradual and non-linear increase of Vp, Vs and density with depth in the first (sedimentary) layer; this simulates sediment compaction and produces more realistic amplitudes of the corresponding RF signals. The third one is a scaling factor δ for the velocity contrast at the Moho. While the first two are straightforward additions, the third new parameter needs further clarification.

At any given iteration of the MCMC simulation, the seismic velocity contrast at the Moho is given by the difference between the sampled velocity for the bottom crustal layer (from its prior distribution) and the predicted velocity for the peridotitic mantle assemblage (from the free-energy minimization solver) at the given P-T-C conditions. Predicted mantle velocities assume a pristine peridotite, with no alteration or hydrated minerals in the assemblage (i.e., the Gibbs free-energy minimization includes only the main nominally anhydrous mineral phases). In reality, shallow mantle lithologies close to the Moho could contain variable amounts of hydrated minerals (e.g., amphiboles, micas; Bucher-Nurminen, 1990), which tend to decrease the velocity and density of the mantle assemblage relative to the "dry" counterpart (e.g., Aizawa et al., 2008). This in turn decreases the velocity contrast at the Moho and the amplitudes of the predicted RFs. Additionally, the model assumes that the Moho contrast is sharp (i.e., a first-order velocity discontinuity between the lower crust and upper mantle) and flat. This neglects potential structural complexities of the Moho, like a transitional velocity gradient, which would affect the observed scattered wave amplitudes (e.g., Eaton, 2006). We therefore allow for "scaled" or "corrected" properties of the shallow, sub-Moho mantle via a scaling factor δ that controls the magnitude of the correction or deviation from predicted thermodynamic values. The factor δ is a free parameter of the inversion that can take values between 0 and 1. A value of 1 means that the predicted thermodynamic properties do not require scaling; values <1 imply a correction proportional to the sampled value of δ. The largest allowed correction corresponds to a value $\delta = 0$ and implies that, for instance, Vs is decreased by a maximum amount of 4%; density and Vp are also consistently corrected.

During the inversion, the thicknesses of all crustal layers were allowed to vary within ±30% of their initial values. Densities were explored within the following ranges: 1,400–2,600 kg/m^3 in the first layer, 2,500–2,850 kg/m^3 in the second layer, 2,700–2,950 kg/m^3 in the third layer and 2,750–3,150 kg/m^3 in the fourth layer. Respective ranges of Vp/Vs were 1.60–2.30, 1.60–1.87, 1.65–1.90 and 1.65–1.90. Since the mantle structure was thoroughly explored in the previous study by Dave et al. (2024), we used their posterior distributions to inform our priors. This resulted in relatively narrow bounds for mantle parameters (e.g., ±45°C for sublithospheric temperatures, ±14 km for the depth of the MLD, ±25 km for the LAB depth, and ±0.8, 1, 5, and 1.3 wt.% for Al_2O_3, FeO, MgO, and CaO, respectively).

6.2.2. North Australian Craton

The numerical domain is bounded by the 127.5/143.0 meridians and the −15.5/−26.0 parallels, and is made up of 23 × 32 (0.5° × 0.5°) adjacent and non-overlapping tesseroidal columns (Figure 8b). The starting model included Moho depths from the most recent AusMoho model (Kennett et al., 2023) and estimates of mechanical lithospheric thickness from Hoggard et al. (2020), which is based on a Vs to temperature conversion from the tomography study of Fishwick & Rawlinson (2012) calibrated using geotherms derived from Australian xenoliths. The initial Moho depths were allowed to vary between −5% and +20% during the inversion. Due to the limited range of periods in the dispersion data set (2.5–60 s), the initial LAB depth was allowed to vary within a relatively narrow range of ±25 km and only the average composition of the lithospheric mantle was considered. For the (unmodeled) volume outside our numerical domain, seismic rays were propagated through the 3D global seismic velocity model of Lu et al. (2019). Summary plots depicting the rays are presented in Figure 8.

Initial crustal stratification is identical to that used for the Superior Craton model (three crystalline layers and one sedimentary layer with depth-dependent properties). Initial values for the total sedimentary thickness were obtained from the OzSeeBase data set (FROGTECH, 2021). The thicknesses of the upper and middle crustal layers were allowed to vary within 30% of the initial value (the thickness of the lower layer was then automatically defined considering the Moho depth). The Vp/Vs ratio of the top (sedimentary) crustal layer was varied between 1.5 and 2.05, while that of the crystalline layers was limited to the range 1.6–1.9. Crustal densities at the top and bottom of the sedimentary layer were allowed to vary in the range 1,400–2,550 kg/m^3 and 2,400–2,860 kg/m^3, respectively. The sampling approach does not allow the bottom density to be smaller than the sampled density at the top of the layer; the interpolation follows a universal compaction (non-linear) profile. Densities at standard conditions of pressure and temperature (i.e., surface conditions) in the upper, middle and lower crystalline layers were varied in the range 2,500–3,000 kg/m^3, 2,800–3,200 kg/m^3 and 2,925–3,200 kg/m^3, respectively. The sampled values were converted into average layer values (used to solve the forward problems) according to the current PT conditions within the layers.

Because of the limited availability of direct information on mantle composition (e.g., mantle xenoliths) and the restricted period range in the dispersion data set, the compositional ranges were based on widely accepted models for the subcratonic lithospheric mantle and bulk Earth geochemistry (Alemayehu et al., 2016; Boyd, 1989; Griffin et al., 1999; Lyubetskaya & Korenaga, 2007; McDonough & Sun, 1995; Salters & Stracke, 2004): Al_2O_3–0.5 to 3.1 wt.%, FeO–6.0 to 8.5 wt.%, MgO–37.0 to 45.0 wt.%, CaO–0.1 to 3.1 wt.% for the lithospheric mantle and Al_2O_3–2.5 to 4.5 wt.%, FeO–6.0 to 8.4 wt.%, MgO–37.0 to 41.0 wt.%, CaO–2.0 to 5.5 wt.% for the sublithospheric mantle.

For clarity and space reasons, we leave the detailed description of all input data sets for the two regions to Text S7 in Supporting Information S1.

7. Results

7.1. Superior Craton

7.1.1. Data Fits

7.1.1.1. Seismic Data

Figure 9 shows four representative examples of fits to RFs and dispersion curves (see Figure 7 for the location of the stations). Maps of phase velocity at periods of 20, 40, 80 and 120 s are shown in Figure 10. Additional plots can be found in Text S4 of Supporting Information S1. The results in these figures clearly demonstrate that the

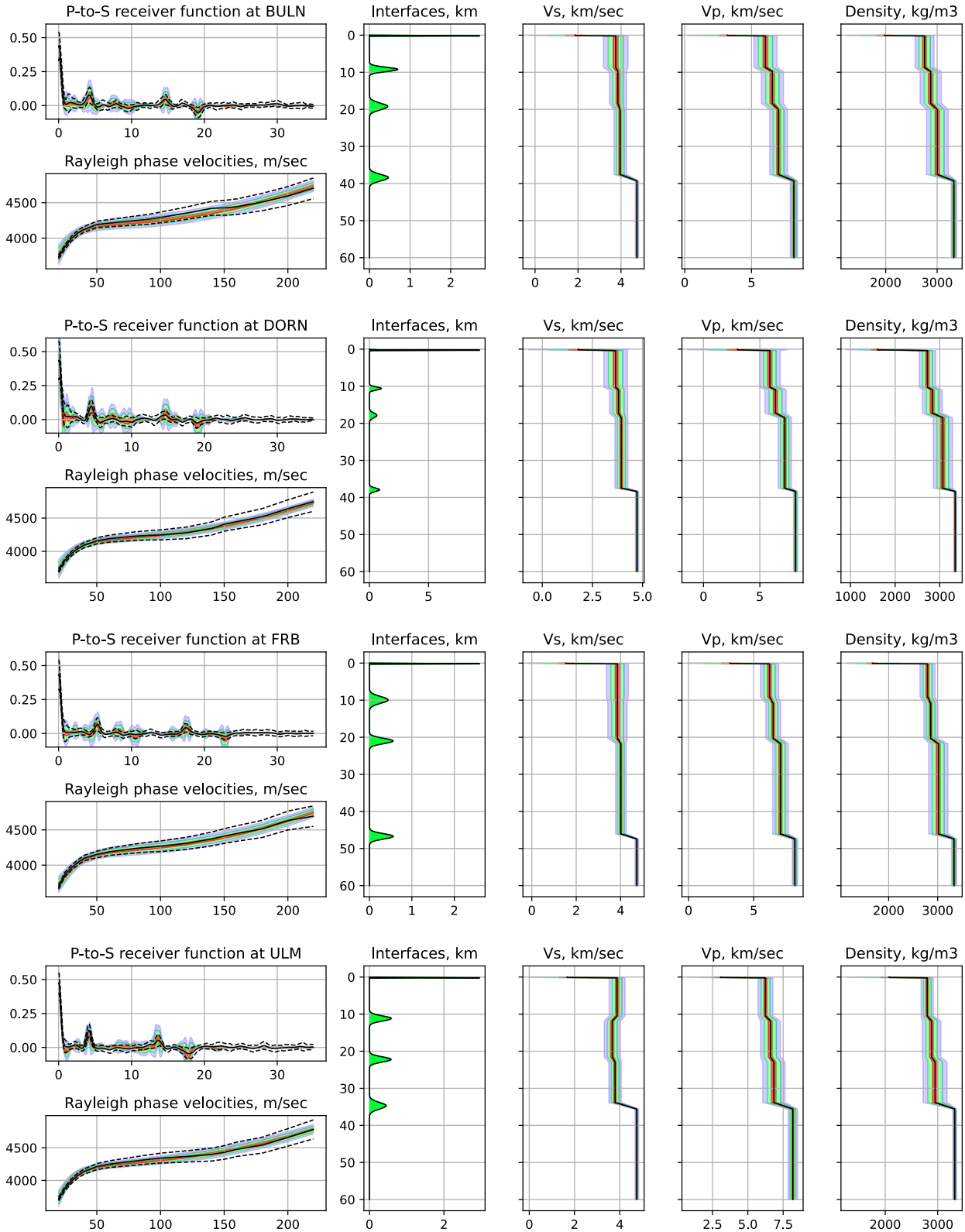

Figure 9. Fits to RFs and dispersion curves for stations BULN, DORN, FRB, and ULM (see location in Figure 7) for the Superior Craton region. Mean RFs and associated uncertainties are denoted by solid black lines and dashed black lines, respectively (same for dispersion curves). Posterior PDFs of predicted data are color-coded as orange (1σ), green (2σ) and gray (3σ). Posterior PDFs for the location of intra-crustal interfaces, Moho and associated Vs, Vp and density profiles are also shown.

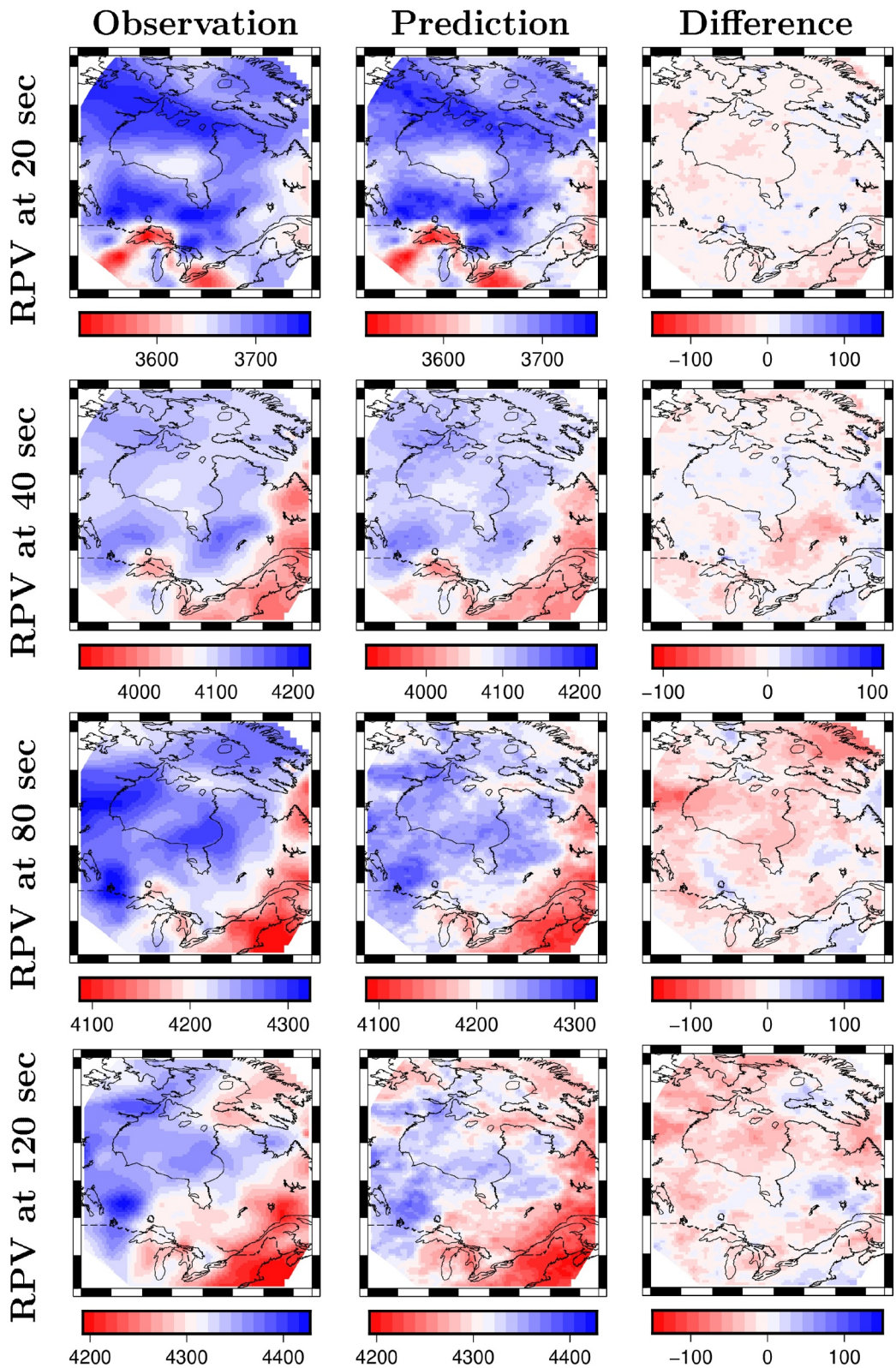

Figure 10. Observed and predicted Rayleigh phase velocities (in m/sec) in the study region; additional periods are shown in Text S4 of Supporting Information S1. The last column shows the absolute difference (predicted-observed) in m/sec. Consider that representative data uncertainties (as 1σ) are ~28, 41, 65 and 87 m/s for periods of 20, 40, 80 and 120 s, respectively. Misfit values are within 1σ of the observed data in >98% of the model.

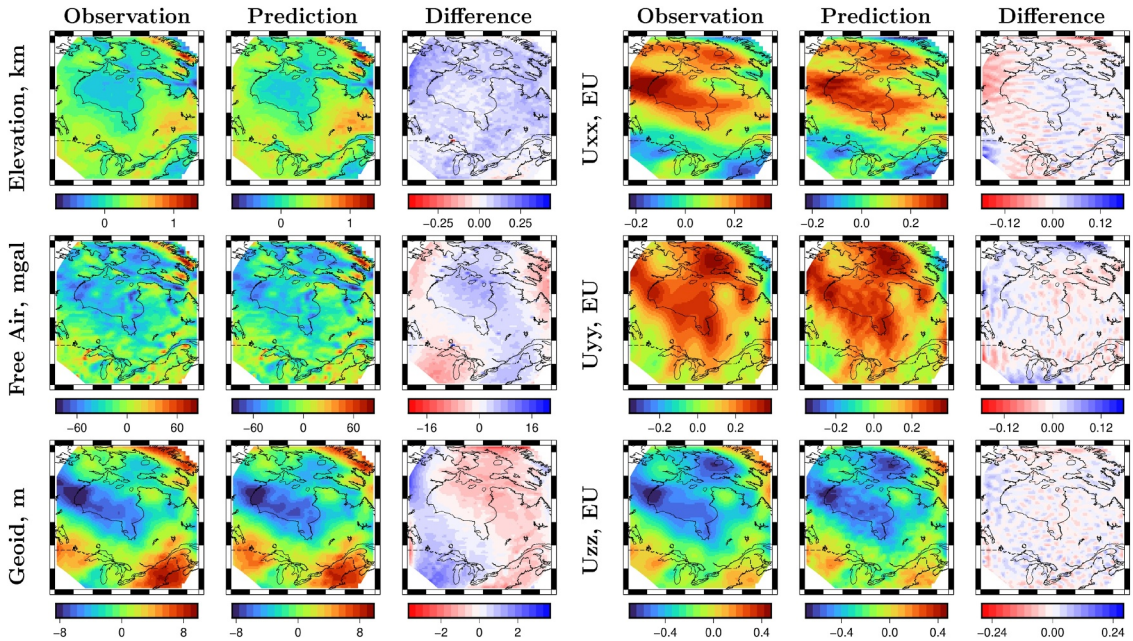

Figure 11. Data fits for elevation (km), free-air anomalies (mgal), geoid anomalies (m) and gravity gradients (Eotvos). Typical uncertainties (defined as 1σ) associated with these data sets are ±150 m for elevation, 5 mgal for free-air anomalies, 0.6 m for geoid height, 0.1 EU for U_{xx} and U_{yy} and 0.2 EU for U_{zz}. The largest discrepancies are found along or near the edges of the numerical domain.

inversion and employed parameterization can satisfactorily reproduce the main features of the seismic data, including converted phases and reverberations associated with crustal discontinuities. Predicted phase velocities (defined as the mean of their posterior PDFs) remain within 1σ of the data uncertainty in most of the domain. The addition of more crustal layers would help improve the fit to the most complex RFs at the cost of increasing the dimensionality of the parameter space. After numerous tests, we deem four layers (one sedimentary and three crystalline) an acceptable compromise between overall data fit quality and parsimony of model parameters.

7.1.1.2. Non-Seismic Data

The fits to elevation, geoid, free-air anomalies and gravity gradients are shown in Figure 11 (additional figures in Text S4 of Supporting Information S1). The maps labeled "prediction" depict the mean of the posterior distributions of predicted data and are almost identical to the data predicted by the mean model (i.e., the 3D model built from the mean of all model parameters). The figure also shows the absolute difference between observed and predicted fields. It is clear from these figures that all non-seismic data sets are satisfactorily fitted, with all the main spatial patterns being explained well by the model. In fact, all non-seismic data sets are reproduced within 2σ of the observed values in the entire numerical domain, and within 1σ in >90% of the studied region. An exception is elevation, which is systematically predicted to be slightly higher than the observed values in the entire study region. This is not surprising given the ongoing post-glacial rebound occurring in this region (e.g., Koohzare et al., 2008); dynamic topography due to sublithospheric flow can also be a factor (Davies et al., 2019). In other words, the present-day thermochemical structure of the lithosphere in this region (as imaged in this study) can only be in partial (non-steady) isostatic equilibrium. Pursuing or forcing better fits to elevation is therefore not justified, as it requires compromising the fits to other observables less sensitive to post-glacial lithospheric rebound and/or dynamic topography.

7.1.2. Lithospheric Architecture

7.1.2.1. Main Crustal Elements

Figures 12 and 13 summarize the main structural features of the model. A more complete set of figures can be found in Text S4 of Supporting Information S1. The first order variation pattern of Moho depth is consistent with previous studies (see Dave et al., 2024, and references therein), although our model shows considerably more

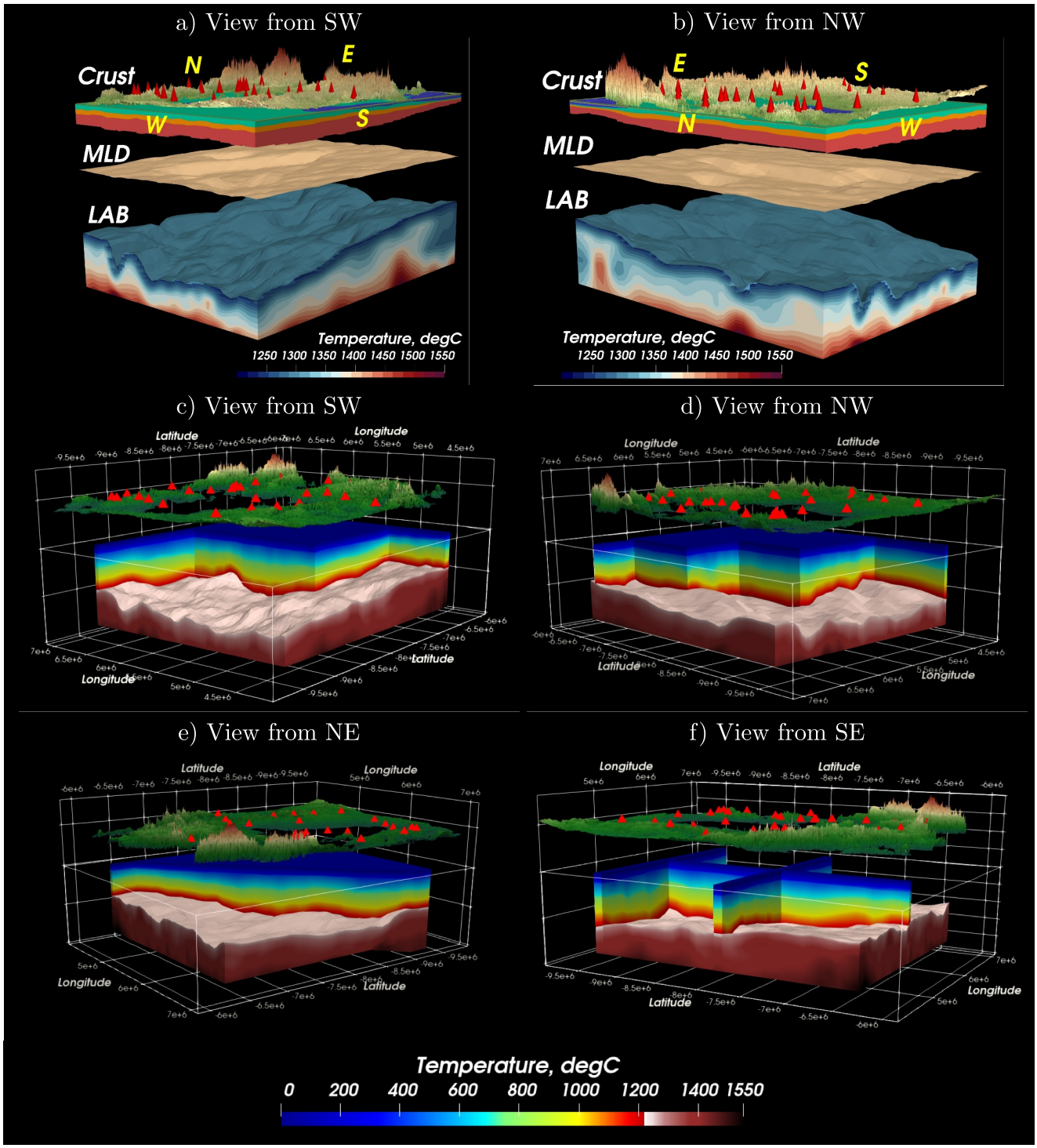

Figure 12. Different views of a 3D rendering of the study region showing crustal layers, mid-lithosphere discontinuity (MLD), lithosphere-asthenosphere boundary (LAB) and sublithospheric temperatures (a, b), and cross-sections of the thermal structure of the lithospheric mantle (c–f). A deepening of the MLD surface corresponds to the location of the craton, while the LAB surface is controlled by the sublithospheric thermal structure and plume-like structures. The crust clearly thickens toward the center of the continent (SW corner), which agrees with geological observations. The red cones indicate locations of the seismic stations used for RF analysis. Depths and topography are exaggerated and the model is plotted in Cartesian coordinates for illustration purposes.

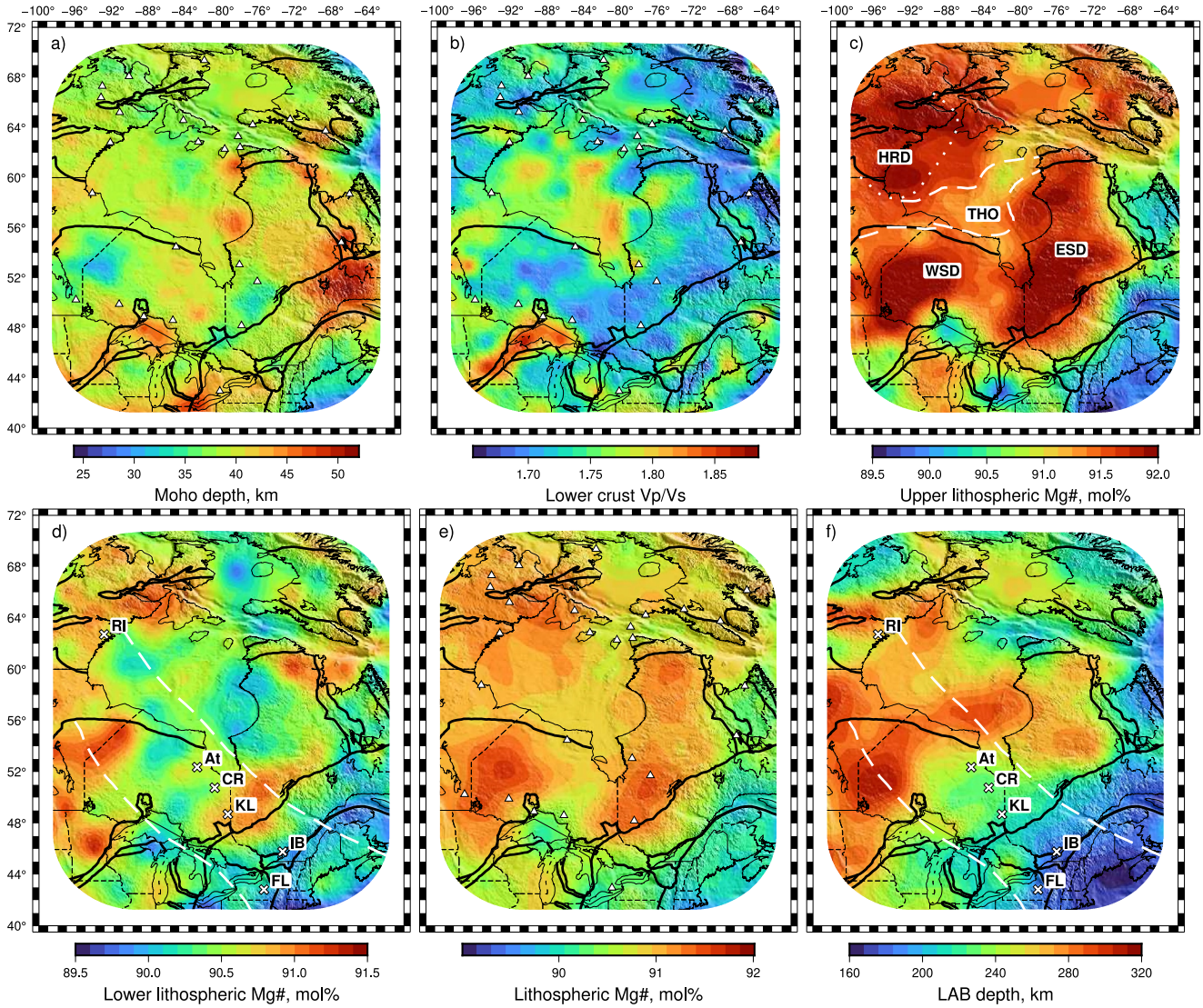

Figure 13. Summary of key model parameters. (a) Moho depth. (b) Vp/Vs ratio in the lower crust. (c) Mg# of the upper lithospheric mantle. HRD, Hearne-Rae domain; THO, Trans-Hudson Orogen; WSD, Western Superior Domain; ESD, Eastern Superior Domain. (d) Mg# of the lower lithospheric mantle. (e) Average Mg# of the entire lithospheric mantle (weighted average of upper and lower layers). (f) LAB depth. RI, Rankin Inlet; At, Attawapiskat; CR, Coral Rapids; KL, Kirkland Lake; IB, Ile Bizard; FL, Finger Lakes. Dashed white lines in (d, f) indicate the bounds of the region containing possible tracks of the Mesozoic Great Meteor hotspot and related magmatism (Heaman et al., 2003; Heaman & Kjarsgaard, 2000). Long dashed lines in (c) indicate the estimated boundaries of the Trans-Hudson Orogen; dotted line in (c) indicates the estimated boundary of the Hearne-Rae domain. White triangles in (a, b, e) denote the locations of seismic stations used for RF modeling.

details and better correlations with major tectonic features than previous models (e.g., Cook et al., 2010; Tesauro et al., 2014; Thompson et al., 2015). A comparison of predicted Moho depths from previous RF studies and from our 3D model is shown in Figure 14.

Four anomalies dominate the amplitude variation in Figure 13a. The first one is the relatively thin crust associated with the 3.0 Ga North Caribou Superterrane (Percival et al., 2006; Stott & Corfu, 1991). This terrane represents a large remnant of continental crust thought to have acted as the core around which smaller terranes accreted during the assembly of the Superior Craton (cf. Percival et al., 2006); it is also a prominent feature in almost all other recovered fields (Figure 13; see also below). A gradual but continuous crustal thinning from Lake Superior toward the North Caribou Superterrane was imaged along seismic line 2 of the Western Superior LITHOPROBE transect (Musacchio et al., 2004), in agreement with our model.

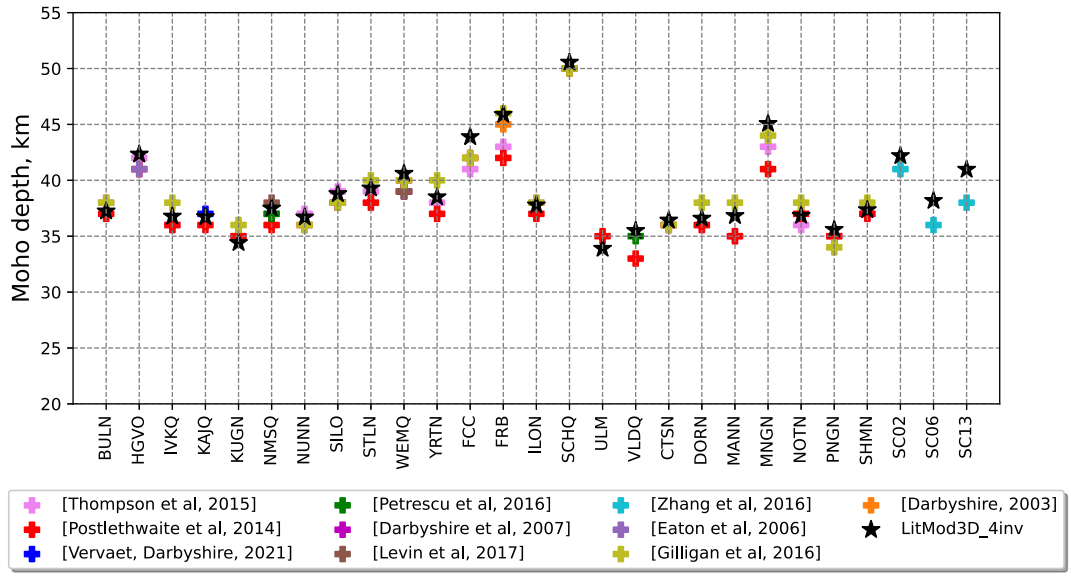

Figure 14. Comparison of Moho depths as estimated from previous seismological studies and from our joint inversion beneath the 27 localities with RF data.

The second anomaly with relatively thin crust is in the Abitibi-Opatica region, southeast of James Bay (Figure 7). Coinciding with a structurally complex region that juxtaposes two Archean units (the granite-greenstone Abitibi and the plutonic Opatica subprovinces), this anomaly seems to be limited to a region bounded by the Kapuskasing complex of dextral faults to the west and a series of major shear zones, reverse and strike-slip faults separating the Opatica and Opinaca domains to the northeast (Figure 7; Mints, 2017; Cleven et al., 2020); the latter also coincides with breaks in the long-wave pattern of magnetic and Bouguer gravity anomalies (Text S4 in Supporting Information S1; Miles & Oneschuk, 2016; Percival et al., 2012).

The remaining two anomalies correspond to regions of relatively thick crust: one within the Grenville province in eastern Canada and along the New Quebec orogen and the other beneath Lake Superior (Figure 13a). While the former coincides with the location (and intersection) of known orogens and high average topography, the latter is located within the northern tip of the Mid-Continent Rift, a region of low topographic relief. Although at first glance these observations contradict a basic tenet of crustal isostasy, a number of previous studies have found evidence of thick and dense crust in this region (e.g., Aleqabi et al., 2023; Behrendt et al., 1990; Grauch, 2023; Hinze & Chandler, 2020; Hutchinson et al., 1990; Stein et al., 2015 and references therein). Our predicted Vp/Vs ratios and densities for the lower section of the crust correspond to those of mafic (dense) materials, such as gabbro and diabase (Figure 13b and Text S4 of Supporting Information S1). This is in agreement with the generally accepted view that mantle-derived melts intruded, underplated and thickened the crust in this region during the rifting event (see references above). We discuss this further in the next section, in connection with our results for mantle composition.

Lastly, we also note that the crust beneath Hudson Bay presents significant anomalies with respect to the surrounding onshore domains. The overall high density of the crystalline crust (Figure S4-1 in Supporing Information S1) explains the low topography and points to a significant contribution of mafic lithologies in the lower portions of the crust. In particular, the largest density anomaly in the western side coincides with large gravity and magnetic anomalies (e.g., Eaton & Darbyshire, 2010). Toward the southeast of the Bay, the Precambrian crust beneath the Belcher Islands is also relatively thick, but comparable to other regions of the Superior Craton. This observation is consistent with previous RF estimates (e.g., Vervaet & Darbyshire, 2022), although we did not model RFs in this location. The crust in this location is also relatively dense (Figure S4-3 in Supporing Information S1), which compensates the buoyancy given by its thickness; the combined effect resulting in shallow bathymetry.

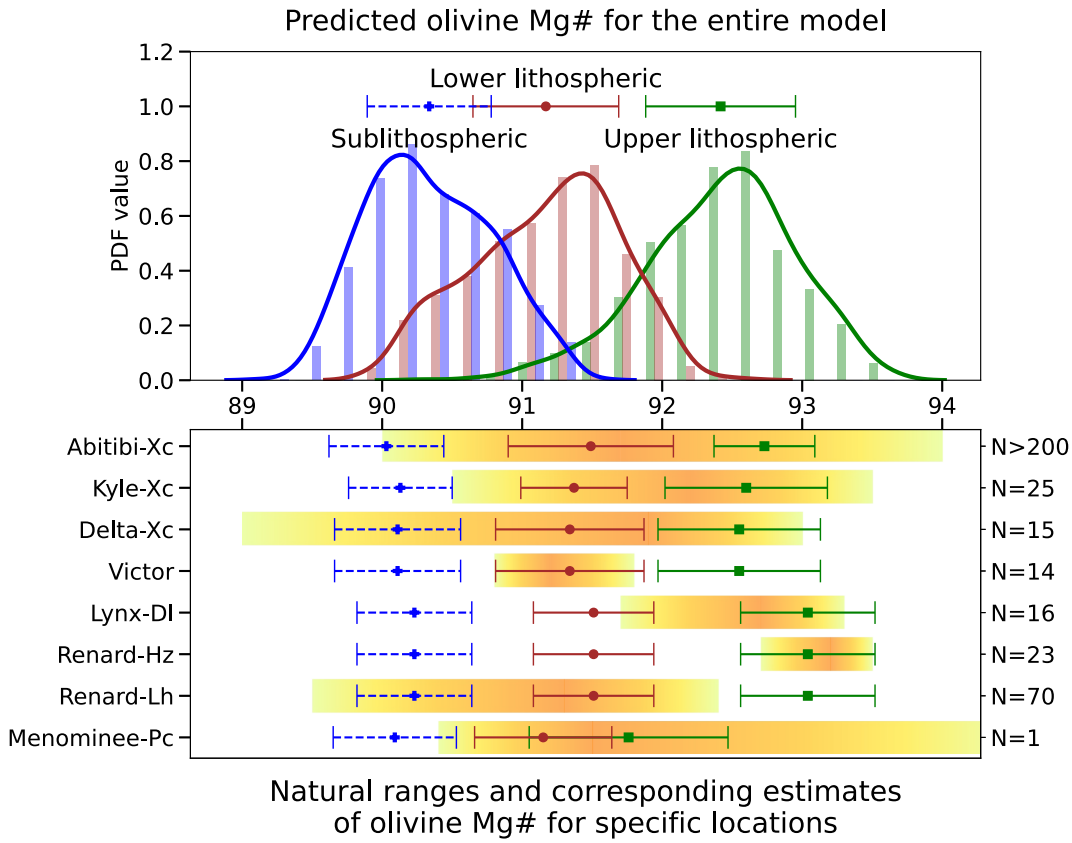

Figure 15. Upper plot: Probability Density Function estimate for the olivine magnesium number Mg# in mantle layers beneath the Superior Craton. Lower plot: the yellowish bars show ranges of natural mantle olivine Mg# from the studied area (Figure 7) with black lines marking the mean values, and predicted means and their standard deviations for the corresponding columns of the inverted model. The sublithospheric olivine Mg# is shown as a dashed line, as it overlaps with the magmatic olivine range composition (Bussweiler et al., 2017) and therefore cannot be reliably distinguished solely by Mg#. Abbreviations: DI, inclusions in diamonds; Xc and Pc, xenocrysts and phenocrysts; Lh and Hz, lherzolite and harzburgite xenoliths; respectively. Data sources: Victor (inclusions in diamonds) (Stachel et al., 2017), Menominee (Xu et al., 2020), Renard (Hunt et al., 2012), Lynx (Van Rythoven et al., 2011), Kyle Lake (Sage, 2000), Abitibi (Lawley et al., 2018). "N" stands for the number of individual grains (each grain could been analyzed several times in different zones).

7.1.2.2. Lithospheric Mantle

Regarding lithospheric thickness and mantle composition, the Grenville and Appalachian Provinces, as well as the Core Zone and Torngat Orogen show the shallowest LAB depths (160–190 km). In fact, the location of the Grenville Front correlates especially well with a transition region of steep gradient in the LAB depth. An even sharper contrast across the Grenville Front is observed in the average composition of the lithospheric mantle (Figure 13e), clearly pointing to identifiable lithospheric units of different nature. This tectonic boundary juxtaposes a relatively fertile lithospheric domain beneath the Grenville and a highly depleted domain beneath the eastern Superior (Figures 13c–13e). Note that while the crust is relatively thick beneath the Grenville, the present-day LAB is relatively shallow.

Another area where the lithosphere is relatively thin is along the Hudson Strait, a failed rift segment associated with the opening of the Labrador Sea. Although this region experienced (trans) extensional tectonics in the initial stages of rifting, crustal thinning seems to have been modest (Pinet et al., 2013). Indeed, while our compositional maps reveal that this elongated tectonic feature correlates with a slight mantle anomaly with respect to the surrounding provinces, there is no prominent shallowing of the Moho. Although deliberately speculative, this "decoupling" between mantle and crustal thinning may be partially explained by the combination of a limited original crustal thinning, post-rift thermal thinning of the lithospheric mantle and a subsequent tectonic inversion (and associated compression) during the Cenozoic (Pinet et al., 2013).

Most of the western Superior, the eastern Superior and the Hudson Bay region exhibit relatively thick and highly depleted lithosphere (i.e., 240 km < LAB < 300 km; Mg# > 92–93); with the highest degrees of depletion in the shallower portions of the lithospheric mantle. An anomaly to this general pattern is found in the southeast Superior (south of James Bay), where the LAB is notably shallower than in the rest of the Superior. As pointed out by previous authors, there is a conspicuous correlation between this region of relatively thin lithosphere and the reconstructed track of the Great Meteor hotspot (Figure 13f; Clouzet et al., 2018; Eaton & Frederiksen, 2007), including the location of Mesozoic kimberlite fields. When looking at the composition of the lithospheric mantle, we acknowledge that the locations of known kimberlitic and kimberlite-related volcanic rocks seem to roughly correlate with regions of lower Mg# compared to the general cratonic/depleted nature of the rest of the Superior Craton. However, we do not observe a clear continuous trend or anomaly that would indicate that large portions of the lithospheric mantle were severely modified/metasomatized by the passage of the Great Meteor hotspot (localized metasomatism is likely, but beyond the resolution of our study). Rather, the distinct compositional domains seem to be reflecting deeper tectonic structures or domains. Interestingly, the separation of the western and eastern blocks of the Superior Craton in terms of mantle composition correlates well with major SW-NE structures between the Kapuskasing complex and those aligned along the western shore of Lake Superior and their continuation to the northwest (Figures 3, 13c and 13e in Harris et al. (2023)). Likewise, the general depletion pattern in the eastern Superior coincides well with the location of three major tectonic terranes: the Rivière Arnaud Terrane, the Bienville/Hudson Bay Terrane and the Opinaca-Opatica-Abitibi domain (Cleven et al., 2020; Leclair, 2008; Mints, 2017).

The internal architecture of the Trans-Hudson Orogen (THO) in the Hudson Bay region is poorly known due to lack of exposure (Eaton & Darbyshire, 2010). Our compositional map of the upper lithosphere shows a clear anomaly separating the highly depleted Hearne-Rae and Superior domains (Figure 13c). This anomaly extends inland into central Canada, following closely the location of major tectonic boundaries separating the north Caribou block from the THO. Despite the relatively coarse resolution for mantle composition, our models clearly show that there are significant portions of the Hearne-Rae and western Superior domains that extend well into Hudson Bay. Similarly, our compositional model can be used to approximate the locations of the boundaries of the THO beneath Hudson Bay (Figure 13c), assuming that the most depleted domains belong to the Hearne-Rae and Superior cratons. Interestingly, our model shows a moderately depleted domain in the western half of Hudson Bay that extends toward the center of the Bay; its composition being slightly less depleted than the surrounding Hearne and Rae cratons. Without favoring any genetic hypothesis, we note that this domain coincides with the proposed Archean fragment of Eaton & Darbyshire (2010), which may have been trapped between the Superior and western Churchill cratons during the THO.

Our map of lithospheric Mg# shows a fertile anomaly beneath the Mid-Continent Rift, especially beneath Lake Superior. As we mentioned in the previous section, this region also exhibits clear evidence of anomalously thick and mafic lower crust, including large accumulations of basaltic material in the lowermost 20 km (e.g., Grauch, 2023; Hinze & Chandler, 2020; Figure 13b). Our results thus suggest that asthenospheric melts not only were produced in significant volumes during the active stage of rifting, but also percolated and reacted with the overlying lithospheric mantle on their way up to crustal levels. This may have imparted the fertile signature (i.e., addition of Ca, Fe, Al) to the lithospheric mantle that we image today. Such mantle refertilization via percolation and reaction of basaltic melts has been reported in other continental areas that experienced significant basaltic magmatism (e.g., Afonso, Rawlinson et al., 2016; Zheng et al., 2015; A. Zhang et al., 2024).

7.2. Comparison With Mantle Xenoliths and Xenocrysts

Predicted magnesium numbers of olivine beneath the Superior Craton are shown in Figure 15. In each mantle layer, Mg# values form a distinct unimodal distribution with the most depleted compositions in the upper lithosphere and the most fertile compositions in the sublithosphere. The overlap between these distributions is minimum at the level of 1 STD, suggesting a distinct vertical stratification of the lithospheric mantle. A similar compositional stratification of the lithospheric mantle has been observed in a number of localities across the Archean cratons of North America (cf. Griffin et al., 2004a). In this context, it is important to emphasize that our method does not use local xenolith information; our results are entirely driven by geophysical observables and thermodynamic modeling.

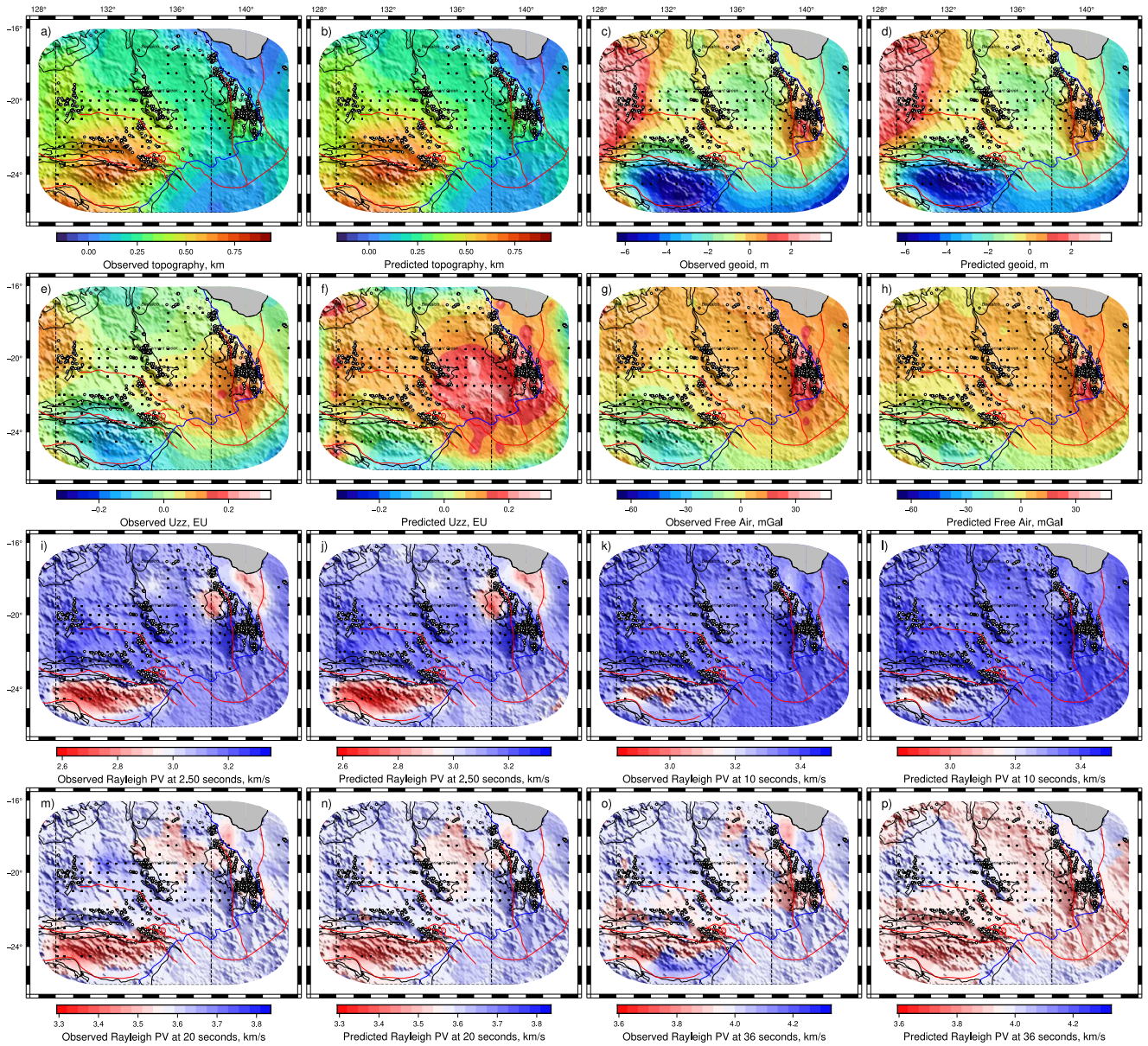

Figure 16. Data fit characteristics of the North Australian Craton model for a representative subset of model outputs. Additional misfit maps can be found in Text S5 of Supporting Information S1.

Comparing the present-day chemical structure retrieved by our inversion with that inferred from mantle xenoliths and xenocrysts can be illustrative, but not straightforward. The youngest kimberlitic volcanism in the region is Jurassic in age (Attawapiskat cluster, 176–180 Ma; Kirkland Lake cluster, 146–160 Ma; Timiskaming cluster, 140–155 Ma; (Heaman & Kjarsgaard, 2000)). Southwest of Attawapiskat, the Kyle Lake kimberlite cluster dates to 1.1 Ga (Sage, 2000). Some other clusters in the region predate the amalgamation of the Superior Craton. Moreover, the highly localized sampling represented by these fields contrasts with the relatively coarse spatial resolution of our inversion. Accordingly, any comparison needs to be taken with great caution.

With these caveats in mind, we note that a recent study of peridotitic xenoliths recovered from the Attawapiskat cluster reported olivines with an average Mg# of 91.9 (Smit et al., 2014). A similar value was reported by Sage (2000) for olivines recovered from the adjacent Kyle Lake cluster. These values are very close to those recovered by our inversion (Figures 13c and 15). Moreover, olivine inclusions found in diamonds from the Victor mine seemed to have been formed in a very narrow range of depths, between 159 and 167 km, with average Mg# of

~91.3 (Stachel et al., 2017); these values are in perfect agreement with our estimates of olivine Mg# at those depths. Further south, the Kirkland Lake field erupted mantle xenoliths around 150–160 Ma ago, which were reported to have olivine Mg# of 91–94 (e.g., Griffin et al., 2004b; Lawley et al., 2018; Meyer et al., 1994), with a clear vertical stratification (more depleted toward shallower depths) and average values around 92.4. Our results are also in good agreement with these observations (Figures 13c and 15).

The age estimate for other kimberlite fields (e.g., Wawa, Lynx, and Renard locations) is around 2.7 Gyr (Stachel et al., 2006), which complicates even further any comparison with our estimates. However, when considering the different depths of equilibration of mantle samples in the Renard field, we observe a striking correlation with our results: olivines from the shallower levels (130–150 km depth) are harzburgitic with average Mg# of ~93, whereas the deeper olivines become lherzolitic, with average Mg# of ~91.5 (Hunt et al., 2012). These observations are reproduced well by our model.

7.3. North Australian Craton

7.3.1. Overall Data Fits

Our preliminary model of the North Australian Craton exhibits a similar level of explanatory power (i.e., simultaneously explains multiple data sets) to that observed in the Superior Craton. The model fits elevation and potential fields (geoid height, free-air anomaly and vertical gravity gradient) within 1σ for >95% of the columns, with maximum misfits located at the edges of the model (Figure 16). The overall fit to phase velocities and receiver functions is also excellent in most of the domain (Figures 16 and 17, Figures S5-11–S5-60 in Supporing Information S1). In terms of body-wave travel times and receiver functions, our final model resulted in an improvement of 15% and 40%, respectively, compared to the starting model.

7.3.2. Lithospheric Architecture

7.3.2.1. Main Crustal Elements

The spatial distribution of modeled parameters broadly matches the major tectonic and geological boundaries within the studied area (Figures 16 and 18). Within the upper crust, the model effectively recovers first-order variations in the distribution of sedimentary basins (Figure 18). The thickness of the first crustal layer in the model maps the distribution of basins. It is 3–4 km thick over the McArthur Basin, mapping less consolidated sediments, and reveals depocentres up to 6 km deep in the Beetaloo and Carrara sub-basins and up to 8 km thick in the Amadeus Basin. Despite the retrieved uncertainties of >1 km in deep basins (Text S6 in Supporting Information S1), our results reveal considerably thinner basins than those mapped in the 2021 OZ SEEBASE data set (FROGTECH, 2021) used as the prior in our inversions. We use multiple geophysical data sets to quantitatively map physical rock properties; this contrasts with the interpretation of geological units adopted by OZ SEEBASE.

Within the mid to lower crust the model reveals considerable variations in density and Vp/Vs (Text S6 of Supporting Information S1). As expected, the average bulk density and Vp/Vs ratio of the entire crystalline crust follows a similar spatial pattern (Figures 18a and 18b), but with smaller amplitudes. High densities beneath Mount Isa and south of Tennant Creek together with high Vp/Vs ratios under Mt Isa support previously inferred underplating in this region (e.g., Drummond & Collins, 1986; Dulfer et al., 2016; Finlayson, 1987). Despite the coherent N–S-trending structures mapped on the surface and in potential fields in the east of the domain (e.g., Gideya suture zone; Figure 7), the mid-to-lower crust in the region north of Mt Isa is noticeably different from that between Mt Isa and the Cork fault, including a considerable jump in crustal thickness. A narrow band of high-density zone in the Arunta region, between the Amadeus and Ngalia basins, corresponds to the well-known crustal-scale thrust structure of the Redbank Deformation Zone, where deep-seated faulting has uplifted lower crustal and possibly mantle material (Goleby et al., 1989). Low bulk crustal densities in the Amadeus Basin are a function of the thick sediments and very low predicted densities of the second crustal layer (down to 2,650 kg/m^3 compared to the average of 2,850 kg/m^3), which likely reflect underlying Neoproterozoic basin stratigraphy. Low crustal densities east of the Tanami coincide with the extent of shallow Moho and low Vp/Vs, likely mapping the distribution of granites (e.g., Roshanravan et al., 2020).

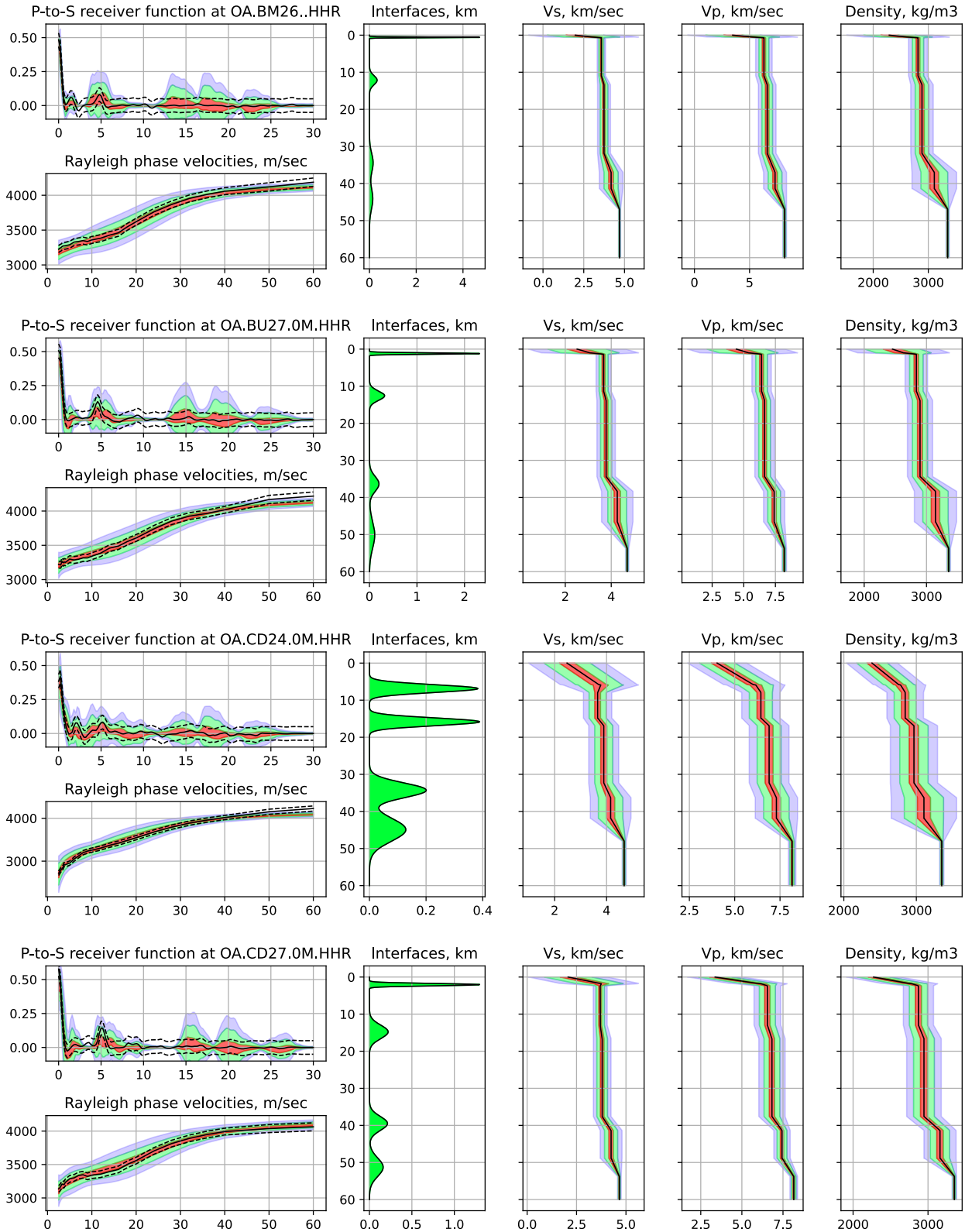

Figure 17. Some representative receiver functions and dispersion curves from the Tanami area (OA.BL26. HHR, OA. BM26.HHR), between the Tanami and Tennant Creek regions (OA.BU27.0M.HHR), and on the southwestern flank of a Mesoproterozoic depocentre known as the Carrara sub-basin in the Mt Isa region (OA. CD24.0M.HHR, OA. CD27.0M.HHR). The red, green, and blue zones outline the 1, 2, and 3 sigma intervals, respectively.

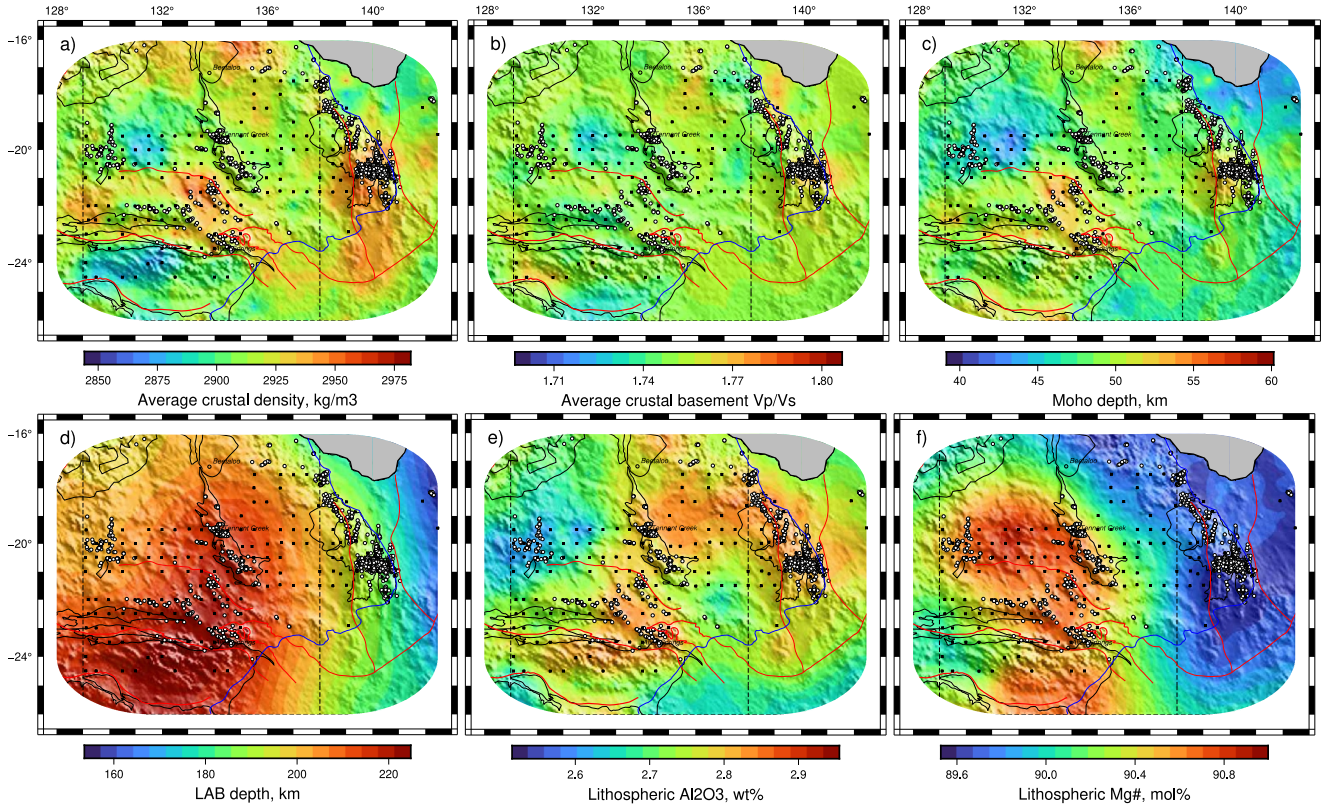

Figure 18. (a) Average crustal density, (b) Average Vp/Vs ratio of the crystalline crust, (c) Moho depth, (d) depth to the LAB, (e) average Al_2O_3 content in the lithospheric mantle, (f) average Mg# of the lithospheric mantle. Black markers indicate the locations of seismic stations. White dots denote mineral deposits. Red lines show major faults. The average crustal density distribution correlates well with the available potential field data (Figure 16) and predicts low density anomalies in the Amadeus and Ngalia basins, and in the Tanami block (See Figure 7 for location). Higher average densities are associated with deep Moho areas (Mount Isa) and upthrust areas (Arunta block). The lithospheric mantle chemical composition defines two broad domains within the North Australian Craton. Depleted compositions occur in the Tanami, close to the geometric center of the Kalkarindji Large Igneous Province, and relatively enriched compositions beneath Mt Isa and McArthur River, Tennant Creek inlier, and Amadeus Basin, the areas with numerous world class deposits and mineral occurrences. The blue line indicates the present-day border of the Great Artesian Basin.

7.3.2.2. Lithospheric Mantle

Our model reveals a fundamental east to west variation in lithospheric mantle composition across the North Australian Craton (Figure 18). In the east the Mg# shows values <89.5, rising to values ≳91 in the center of the craton. Our Mg# values match analyses from the Webb Ultramafic Lamprophyre field which intrudes along the western edge of the model and has an olivine Mg# of 88–91 where our model returns a bulk medium estimate of 90 (Sudholz et al., 2023). The pattern we observe is also roughly similar to that inferred by Tesauro et al. (2020), who estimated the most depleted mantle (Mg# up to 90.7) in the central parts of the North Australian Craton, surrounded by relatively more fertile compositions. In detail, the Mt Isa and McArthur regions show the most juvenile lithospheric mantle signature, characterized by low Mg# and highest Al_2O_3 wt%. This is consistent with modeled low degrees of partial melting in the formation of the extensive mafic volcanism which is commonly considered to be the source of metals within this highly endowed mineral province (Champion et al., 2022; Klocking et al., 2020). The most depleted mantle is found just east of the Tanami gold field corresponding with high Mg# and low Al_2O_3 wt% values. This signature is consistent with an Archean lithospheric mantle and the only known distribution of Archean rocks in the study area (Griffin et al., 2008). Interestingly, the extent of the outcropping Tennant Creek region lies precisely between two contrasting lithospheric blocks. To the east, the Murphy block is characterized by high Al_2O_3 and low Mg# and to the west the Tanami region is characterized by the inverse, implying these two regions have experienced fundamentally different geological histories. We note that the locations of known mineral deposits tend to correlate with both marginal regions of highly depleted blocks and regions with fertile mantle (also with high Vs in the lower crust, Text S6 in Supporting Information S1). When

combined with additional tectonic and geological proxies, these observations become informative in exploration frameworks.

This preliminary application of MTT across the North Australian Craton demonstrates the potential of our approach to resolve lithospheric architecture at a sub-cratonic scale. The resolution of spatially coherent lithospheric blocks over a region where most basement rocks are concealed beneath younger sedimentary basins demonstrates the power of multiparameter models in unraveling geological structure under cover and guiding future exploration efforts.

8. Concluding Remarks

Ongoing progress in the quality, quantity, and global coverage of seismic and satellite data sets, coupled with advances in thermodynamic databases and computational methodologies for tackling intricate forward problems, present new opportunities for developing more comprehensive and reliable subsurface models through formal data integration/fusion techniques. Such integrative models of the physical state of the subsurface (i.e., temperature, composition, stress state, fluid fraction) provide fundamental insights into the constitution and evolution of the Earth's interior. They are also becoming essential data-fusion tools for advancing greenfields exploration of critical minerals, deep geothermal energy exploration, and informing ice-melting models, particularly regarding basal heat flow beneath large ice caps (e.g., Antarctica, Greenland).

Multi-observable Thermochemical Tomography (MTT) is a joint inversion platform designed to harness the combined sensitivities of multiple data sets to image the physical state of the Earth's interior with thorough uncertainty quantification. Since its introduction just over a decade ago (Afonso, Fullea, Griffin et al., 2013, Afonso, Fullea, Yang et al., 2013), MTT has significantly advanced in both conceptualization and numerical implementation. This paper presented an updated MTT framework and assessed its strengths and limitations in the context of thermochemical imaging of the lithosphere. We used complex synthetic models to study the sensitivities of both independent and combined data sets and the corresponding reliability of the retrieved structure. Although our software (*LitMod3D_4INV*) can integrate additional data sets, we particularly focused on joint inversions of gravity anomalies, the Marussi tensor (gravity gradients), geoid anomalies, Rayleigh-wave dispersion curves, P-wave receiver functions, absolute elevation, surface heat flow and absolute travel times from (local and teleseismic) P-wave and S-wave phases. We demonstrated that judicious combinations of these data sets can constrain complex thermochemical structures in the lithosphere and sublithospheric upper mantle with resolutions and reliability relevant to greenfields exploration programs for minerals and energy. Higher resolution studies are also possible, but were not explored in this work.

With this information, we applied the method to two different groups of data sets in two different cratonic regions: the Superior Craton (Canada) and the North Australian Craton. The resulting thermochemical models exhibit an exceptional capacity to simultaneously fit all inverted data sets and showcase the potential of MTT to (a) serve as an integration platform for inverting and interpreting multiple observables, (b) uncover structural and evolutionary connections between the crust, lithospheric mantle, and asthenosphere, (c) provide reliable and interpretable subsurface models in terms of their physical nature, and (d) provide valuable information for guiding exploration efforts for clean energy and critical minerals.

Looking forward, we plan to expand the capability and improve the reliability of MTT by implementing (a) a more comprehensive use of waveform information and (b) magnetic susceptibility/anomalies for Curie point estimates; these are topics of forthcoming publications.

Conflict of Interest

The authors declare no conflicts of interest relevant to this study.

Data Availability Statement

The software and the models discussed in this manuscript are available on Zenodo (Fomin et al., 2025). The data on which this article is based are available in Afonso et al. (2019), (Balmino et al., 2011; Bonvalot et al., 2012; Kvas et al., 2021; NOAA, 2022), Dave et al. (2024), (Geoscience Australia, 2021; Gorbatov et al., 2019, 2020; Hassan et al., 2020; Hejrani et al., 2020; International Seismological Centre, 2023; Kennett et al., 2023; Lu

et al., 2019). The software used to prepare the data is described in Martinec (2014), (Ligorria & Ammon, 1999). Figures were prepared using Paraview (Ahrens et al., 2005), GMT 6 (Wessel et al., 2019), and Matplotlib (Hunter, 2007).

Acknowledgments
IF, JCA, AG, BH, MWH and KC acknowledge funding from EFTF—Exploring for the Future program of Geoscience Australia. JCA was partially supported by the ESA Grant 4D-Earth. SH was partially supported by Australian Research Council Discovery Project Grant 210102196. FAD and RD were supported by the Natural Sciences and Engineering Research Council of Canada (NSERC) through their Discovery Grant, Canada Research Chair and Alliance programs; the Alliance program also included funding from De Beers Canada.

References

Afonso, J. C., Ben Mansour, W., O'Reilly, S. Y., Griffin, W. L., Salajegheh, F., Foley, S., et al. (2022). Thermochemical structure and evolution of Cratonic lithosphere in central and Southern Africa. *Nature Geoscience*, *15*, 1–6. https://doi.org/10.1038/s41561-022-00929-y

Afonso, J. C., Fullea, J., Griffin, W. L., Yang, Y., Jones, A. G., Connolly, J. A. D., & O'Reilly, S. Y. (2013). 3-D multi-observable probabilistic inversion for the compositional and thermal structure of the lithosphere and upper mantle. I: A priori petrological information and geophysical observables. *Journal of Geophysical Research: Solid Earth*, *118*(5), 2586–2617. https://doi.org/10.1002/jgrb.50124

Afonso, J. C., Fullea, J., Yang, Y., Connolly, J. A. D., & Jones, A. G. (2013). 3-D multi-observable probabilistic inversion for the compositional and thermal structure of the lithosphere and upper mantle. II: General methodology and resolution analysis. *Journal of Geophysical Research: Solid Earth*, *118*(4), 1650–1676. https://doi.org/10.1002/JGRB.50123

Afonso, J. C., Moorkamp, M., & Fullea, J. (2016a). Imaging the lithosphere and upper mantle: Where we are at and where we are going. In M. Moorkamp, P. G. Lelièvre, N. Linde, & A. Khan (Eds.), *Integrated imaging of the Earth: Theory and applications* (pp. 191–218). Wiley Online Library. https://doi.org/10.1002/9781118929063.ch10

Afonso, J. C., Ranalli, G., Fernàndez, M., Griffin, W. L., O'Reilly, S. Y., & Faul, U. H. (2010). On the Vp/Vs-Mg# correlation in mantle peridotites: Implications for the identification of thermal and compositional anomalies in the upper mantle. *Earth and Planetary Science Letters*, *289*(3), 606–618. https://doi.org/10.1016/j.epsl.2009.12.005

Afonso, J. C., Rawlinson, N., Yang, Y., Schutt, D. L., Jones, A. G., Fullea, J., & Griffin, W. L. (2016b). 3-D multiobservable probabilistic inversion for the compositional and thermal structure of the lithosphere and upper mantle: III. Thermochemical tomography in the Western-central U.S. *Journal of Geophysical Research: Solid Earth*, *121*(10), 7337–7370. https://doi.org/10.1002/2016JB013049

Afonso, J. C., Salajegheh, F., Szwillus, W., Ebbing, J., & Gaina, C. (2019). A global reference model of the lithosphere and upper mantle from joint inversion and analysis of multiple data sets [Dataset]. *Geophysical Journal International*, *217*(3), 1602–1628. https://doi.org/10.1093/gji/ggz094

Afonso, J. C., Zlotnik, S., & Díez, P. (2015). An efficient and general approach for implementing thermodynamic phase equilibria information in geophysical and geodynamic studies. *Geochemistry, Geophysics, Geosystems*, *16*(10), 3767–3777. https://doi.org/10.1002/2015GC006031

Ahmad, M., & Scrimgeour, I. R. (2013). Geology and mineral resources of the Northern Territory. In M. Ahmad & T. Munson (Eds.), *Geology and mineral resources of the Northern Territory* (Vol. 5, pp. 2:1–2:16). Northern Territory Geological Survey, Special Publication.

Ahrens, J. P., Geveci, B., & Law, C. C. (2005). ParaView: An end-user tool for large-data visualization, *The visualization handbook* [Software]. In C. D. Hansen, & C. R. Johnson (Eds.), Academic Press / Elsevier. https://doi.org/10.1016/B978-012387582-2/50038-1

Aizawa, Y., Barnhoorn, A., Faul, U. H., Fitz Gerald, J. D., Jackson, I., & Kovács, I. (2008). Seismic properties of Anita Bay Dunite: An exploratory study of the influence of water. *Journal of Petrology*, *49*(4), 841–855. https://doi.org/10.1093/petrology/egn007

Alemayehu, M., Zhang, H.-F., Zhu, B., Fentie, B., Abraham, S., & Haji, M. (2016). Petrological constraints on evolution of continental lithospheric mantle beneath the northwestern Ethiopian plateau: Insight from mantle xenoliths from the Gundeweyn area, East Gojam, Ethiopia. *Lithos*, *240–243*, 295–308. https://doi.org/10.1016/j.lithos.2015.11.021

Aleqabi, G. I., Wysession, M. E., Wiens, D. A., Shen, W., Van der Lee, S., Darbyshire, F. A., et al. (2023). Joint inversion of SPREE receiver functions and surface wave dispersion curves for 3-D crustal and upper mantle structure beneath the U.S. midcontinent rift. *Journal of Geophysical Research: Solid Earth*, *128*(12), e2023JB026771. https://doi.org/10.1029/2023JB026771

Balmino, G., Vales, N., Sylvain, B., & Briais, A. (2011). Spherical harmonic modelling to ultra-high degree of Bouguer and isostatic anomalies [Dataset]. *Journal of Geodesy*, *86*(7), 499–520. https://doi.org/10.1007/s00190-011-0533-4

Behrendt, J. C., Hutchinson, D. R., Lee, M., Thornber, C. R., Tréhu, A., Cannon, W. F., & Green, A. S. P. (1990). GLIMPCE seismic reflection evidence of deep-crustal and upper-mantle intrusions and magmatic underplating associated with the Midcontinent rift system of North America. *Tectonophysics*, *173*(1), 595–615. https://doi.org/10.1016/0040-1951(90)90248-7

Berkhout, A. J. (2014). Review paper: An outlook on the future of seismic imaging, Part I: Forward and reverse modelling. *Geophysical Prospecting*, *62*(5), 911–930. https://doi.org/10.1111/1365-2478.12161

Bodin, T., Sambridge, M., Gallagher, K., & Rawlinson, N. (2012). Transdimensional inversion of receiver functions and surface wave dispersion. *Journal of Geophysical Research*, *117*(B2). https://doi.org/10.1029/2011JB008560

Bonvalot, S., Balmino, G., Briais, A., Kuhn, M., Peyrefitte, A., Vales, N., et al. (2012). World gravity map [Dataset]. *Commission for the Geological Map of the World*. https://doi.org/10.14682/2012GRAVISOST

Boyd, F. R. (1989). Compositional distinction between oceanic and cratonic lithosphere. *Earth and Planetary Science Letters*, *96*(1), 15–26. https://doi.org/10.1016/0012-821X(89)90120-9

Braz, C., Zahirovic, S., Salles, T., Flament, N., Harrington, L., & Müller, R. D. (2021). Modelling the role of dynamic topography and eustasy in the evolution of the great Artesian Basin. *Basin Research*, *33*(6), 3378–3405. https://doi.org/10.1111/bre.12606

Brooks, S., Gelman, A., Jones, G., & Meng, X.-L. (2011). *Handbook of Markov Chain Monte Carlo*. CRC Press.

Bucher-Nurminen, K. (1990). Transfer of mantle fluids to the lower continental crust: Constraints from mantle mineralogy and Moho temperature. *Chemical Geology*, *83*(3), 249–261. https://doi.org/10.1016/0009-2541(90)90283-D

Bussweiler, Y., Brey, G. P., Pearson, D. G., Stachel, T., Stern, R. A., Hardman, M. F., et al. (2017). The aluminum-in-olivine thermometer for mantle peridotites – Experimental versus empirical calibration and potential applications. *Lithos*, *272–273*, 301–314. https://doi.org/10.1016/j.lithos.2016.12.015

Champion, D. C., Huston, D. L., Bastrakov, E., Siégel, C., Thorne, J., Gibson, G. M., et al. (2022). Alteration of mafic igneous rocks of the southern McArthur basin: Comparison with the Mount Isa region and implications for basin-hosted base metal deposits. In K. Czarnota, I. C. Roach, S. T. Abbott, M. Haynes, N. Kositcin, A. Ray, & E. Slatter (Eds.), *Exploring for the future: Extended abstracts*. https://doi.org/10.11636/134206

Cleven, N. R., Guilmette, C., Davis, D. W., & Côté-Roberge, M. (2020). Geodynamic significance of Neoarchean metasedimentary belts in the Superior Province: Detrital zircon U-Pb LA-ICP-MS geochronology of the Opinaca and La Grande subprovinces. *Precambrian Research*, *347*, 105819. https://doi.org/10.1016/j.precamres.2020.105819

Clouzet, P., Masson, Y., & Romanowicz, B. A. (2018). Box Tomography: First application to the imaging of upper-mantle shear velocity and radial anisotropy structure beneath the North American continent. *Geophysical Journal International*, *213*(3), 1849–1875. https://doi.org/10.1093/gji/ggy078

Clowes, R. M. (2010). Initiation, development, and benefits of Lithoprobe — Shaping the direction of Earth science research in Canada and beyond. *Canadian Journal of Earth Sciences*, *47*(4), 291–314. https://doi.org/10.1139/E09-074

Connolly, J. A. D. (2009). The geodynamic equation of state: What and how. *Geochemistry, Geophysics, Geosystems*, *10*(10). https://doi.org/10.1029/2009GC002540

Connolly, J. A. D., & Khan, A. (2016). Uncertainty of mantle geophysical properties computed from phase equilibrium models. *Geophysical Research Letters*, *43*(10), 5026–5034. https://doi.org/10.1002/2016GL068239

Cook, F., White, D. J., Jones, A. G., Eaton, D. W. S., Hall, J., & Clowes, R. M. (2010). How the crust meets the mantle: Lithoprobe perspectives on the Mohorovičić discontinuity and crust-mantle transition. *Canadian Journal of Earth Sciences*, *47*(4), 315–351. https://doi.org/10.1139/E09-076

Corrigan, D., Pehrsson, S., Wodicka, N., & de Kemp, E. (2009). The palaeoproterozoic Trans-Hudson orogen: A prototype of modern accretionary processes. *Geological Society, London, Special Publications*, *327*(1), 457–479. https://doi.org/10.1144/SP327.19

Corrigan, D., Wodicka, N., McFarlane, C., Lafrance, I., Van Rooyen, D., Bandyayera, D., & Bilodeau, C. (2018). Lithotectonic framework of the core zone. *Southeastern Churchill Province Geoscience Canada*, *45*, 1–24. https://doi.org/10.12789/geocanj.2018.45.128

Czarnota, K., Jaques, A. L., Huston, D. L., Teh, M., Richards, F. D., Hoggard, M. J., et al. (2020). Minerals on the edge: Sediment-hosted base metal endowment above steps in lithospheric thickness. In K. Czarnota, I. C. Roach, S. T. Abbott, M. Haynes, N. Kositcin, A. Ray, & E. Slatter (Eds.), *Exploring for the future: Extended abstracts* (pp. 1–4). https://doi.org/10.11636/134991

Czarnota, K., Roach, I., Abbott, S., Haynes, M., Kositcin, N., Ray, A., et al. (2020). Exploring for the future: Advancing the search for groundwater, energy and mineral resources. In K. Czarnota, I. C. Roach, S. T. Abbott, M. Haynes, N. Kositcin, A. Ray, & E.Slatter, *Exploring for the future* (pp. 1–14). Extended abstracts. https://doi.org/10.11636/140115

Czarnota, K., Roberts, G. G., White, N. J., & Fishwick, S. (2014). Spatial and temporal patterns of Australian dynamic topography from river profile modeling. *Journal of Geophysical Research: Solid Earth*, *119*(2), 1384–1424. https://doi.org/10.1002/2013JB010436

Dave, R., Darbyshire, F. A., Afonso, J. C., & Fomin, I. (2024). Thermochemical structure of the superior craton and environs: Implications for the evolution and preservation of cratonic lithosphere [Dataset]. *Geochemistry, Geophysics, Geosystems*, *25*(6). https://doi.org/10.1029/2024GC011454

Davies, D. R., Valentine, A. P., Kramer, S. C., Rawlinson, N., Hoggard, M. J., Eakin, C. M., & Wilson, C. R. (2019). Earth's multi-scale topographic response to global mantle flow. *Nature Geoscience*, *12*(10), 845–850. https://doi.org/10.1038/s41561-019-0441-4

Deschamps, F., Trampert, J., & Snieder, R. (2002). Anomalies of temperature and iron in the uppermost mantle inferred from gravity data and tomographic models. *Physics of the Earth and Planetary Interiors*, *129*(3–4), 245–264. https://doi.org/10.1016/S0031-9201(01)00294-1

Dosso, S. E., & Wilmut, M. J. (2006). Data uncertainty estimation in matched-field geoacoustic inversion. *IEEE Journal of Oceanic Engineering*, *31*(2), 470–479. https://doi.org/10.1109/JOE.2006.875099

Drummond, B. J., & Collins, C. D. N. (1986). Seismic evidence for underplating of the lower continental crust of Australia. *Earth and Planetary Science Letters*, *79*(3), 361–372. https://doi.org/10.1016/0012-821X(86)90192-5

Dulfer, H., Skirrow, R. G., Champion, D. C., Highet, L. M., Czarnota, K., Coghlan, R., & Milligan, P. (2016). *Potential for intrusion-hosted Ni-Cu-PGE sufide deposits in Australia: A continental-scale analysis of mineral system prospectivity*. (Tech. Rep.). Geoscience Australia. https://doi.org/10.11636/Record.2016.001

Eaton, D. W. S. (2006). Multi-genetic origin of the continental Moho: Insights from LITHOPROBE. *Terra Nova*, *18*(1), 34–43. https://doi.org/10.1111/j.1365-3121.2005.00657.x

Eaton, D. W. S., & Darbyshire, F. A. (2010). Lithospheric architecture and tectonic evolution of the Hudson Bay region. *Tectonophysics*, *480*(1), 1–22. https://doi.org/10.1016/j.tecto.2009.09.006

Eaton, D. W. S., & Frederiksen, A. W. (2007). Seismic evidence for convection-driven motion of the North American plate. *Nature*, *446*(7134), 428–431. https://doi.org/10.1038/nature05675

Fichtner, A., Trampert, J., Cupillard, P., Saygin, E., Taymaz, T., Capdeville, Y., & Villaseñor, A. (2013). Multiscale full waveform inversion. *Geophysical Journal International*, *194*(1), 534–556. https://doi.org/10.1093/gji/ggt118

Finlayson, D. (1987). Seismic features of Proterozoic crust in Northern Australia and their evolution. In *Proterozic lithospheric evolution* (pp. 99–113). American Geophysical Union (AGU). https://doi.org/10.1029/GD017p0099

Fishwick, S., & Rawlinson, N. (2012). 3-D structure of the Australian lithosphere from evolving seismic datasets. *Australian Journal of Earth Sciences*, *59*(6), 809–826. https://doi.org/10.1080/08120099.2012.702319

Fomin, I., Afonso, J. C., Salajegheh, F., Gorbatov, A., Dave, R., Darbyshire, F. A., et al. (2025). LitMod3D_4inv v3.4.9 + models (v3.4.9-models) [Software], [Dataset]. https://doi.org/10.5281/zenodo.15465065

Forte, A. M., & Mitrovica, J. X. (2001). Deep-mantle high-viscosity flow and thermochemical structure inferred from seismic and geodynamic data. *Nature*, *410*(6832), 1049–1056. https://doi.org/10.1038/35074000

Forte, A. M., & Perry, H. K. C. (2000). Geodynamic evidence for a chemically depleted continental tectosphere. *Science*, *290*(5498), 1940–1944. https://doi.org/10.1126/science.290.5498.1940

FROGTECH. (2021). Phanerozoic OZ SEEBASE v2 GIS [Dataset]. *Bioregional Assessment Source*. Retrieved from http://data.bioregionalassessments.gov.au/dataset/26e0fbd9-d8d0-4212-be52-ca317e27b3bd

Geoscience Australia. (2021). Geoscience Australia earthquake catalogue [Dataset]. Retrieved from https://pid.geoscience.gov.au/dataset/ga/144691

Gibson, G. M., Meixner, A. J., Withnall, I. W., Korsch, R. J., Hutton, L. J., Jones, L. E. A., et al. (2016). Basin architecture and evolution in the Mount Isa mineral province, northern Australia: Constraints from deep seismic reflection profiling and implications for ore genesis. *Ore Geology Reviews*, *76*, 414–441. https://doi.org/10.1016/j.oregeorev.2015.07.013

Glass, L. M., & Phillips, D. (2006). The Kalkarindji continental flood basalt province: A new Cambrian large igneous province in Australia with possible links to faunal extinctions. *Geology*, *34*(6), 461–464. https://doi.org/10.1130/G22122.1

Godey, S., Deschamps, F., Trampert, J., & Snieder, R. (2004). Thermal and compositional anomalies beneath the North American continent. *Journal of Geophysical Research*, *109*(B1). https://doi.org/10.1029/2002JB002263

Goleby, B. R., Shaw, R. D., Wright, C., Kennett, B. L. N., & Lambeck, K. (1989). Geophysical evidence for "thick-skinned" crustal deformation in central Australia. *Nature*, *337*(6205), 325–330. https://doi.org/10.1038/337325a0

Gorbatov, A., Czarnota, K., Hejrani, B., Haynes, M., Hassan, R., Medlin, A., et al. (2019). AusArray: Towards updatable, national high-resolution seismic velocity models of the lithosphere [Dataset], *Exploring for the future: Extended abstracts*. In K. Czarnota, I. C. Roach, S. T. Abbott, M. Haynes, N. Kositcin, A. Ray, & E. Slatter (Eds.), (pp. 1–4). https://doi.org/10.1080/22020586.2019.12073163

Gorbatov, A., Fukao, Y., & Widiyantoro, S. (2001). Application of a three-dimensional ray-tracing technique to global P, PP and Pdiff traveltime tomography. *Geophysical Journal International*, *146*(3), 583–593. https://doi.org/10.1046/j.0956-540x.2001.01487.x

Gorbatov, A., Medlin, A., Kennett, B. L. N., Doublier, M. P., Czarnota, K., Fomin, I., et al. (2020). Moho variations in northern Australia [Dataset], *Exploring for the future: Extended abstracts*. In K. Czarnota, I. C. Roach, S. T. Abbott, M. Haynes, N. Kositcin, A. Ray, & E. Slatter (Eds.), (pp. 1–4). Geoscience Australia. https://doi.org/10.11636/135179

Gorbatov, A., Widiyantoro, S., Fukao, Y., & Gordeev, E. (2000). Signature of remnant slabs in the North Pacific from P-wave tomography. *Geophysical Journal International*, *142*(1), 27–36. https://doi.org/10.1046/j.1365-246x.2000.00122.x

Grauch, V. J. S. (2023). *Compressional-wave seismic velocity, bulk density, and their empirical relations for geophysical modeling of the Midcontinent rift system in the Lake Superior region*. (Tech. Rep.). US Geological Survey. https://doi.org/10.3133/sir20235061

Griffin, W. L., Belousova, E. A., Shee, S., Pearson, N. J., & O'Reilly, S. Y. (2004). Archean crustal evolution in the northern Yilgarn craton: U–Pb and Hf-isotope evidence from detrital zircons. *Precambrian Research*, *131*(3–4), 231–282. https://doi.org/10.1016/j.precamres.2003.12.011

Griffin, W. L., Doyle, B. J., Ryan, C. G., Pearson, N. J., O'Reilly, S. Y., Davies, R., et al. (1999). Layered Mantle lithosphere in the Lac de Gras area, slave craton: Composition, structure and origin. *Journal of Petrology*, *40*(5), 705–727. https://doi.org/10.1093/petroj/40.5.705

Griffin, W. L., O'Reilly, S. Y., Afonso, J. C., & Begg, G. C. (2008). The composition and evolution of lithospheric mantle: A Re-evaluation and its tectonic implications. *Journal of Petrology*, *50*(7), 1185–1204. https://doi.org/10.1093/petrology/egn033

Griffin, W. L., O'Reilly, S. Y., Doyle, B. J., Pearson, N. J., Coopersmith, H., Kivi, K., et al. (2004). Lithosphere mapping beneath the North American plate. *Lithos*, *77*(1), 873–922. https://doi.org/10.1016/j.lithos.2004.03.034

Guo, Z., Afonso, J. C., Qashqai, T. M., Yang, Y., & Chen, Y. J. (2016). Thermochemical structure of the North China craton from multi-observable probabilistic inversion: Extent and causes of cratonic lithosphere modification. *Gondwana Research*, *37*, 252–265. https://doi.org/10.1016/j.gr.2016.07.002

Haario, H., Saksman, E., & Tamminen, J. (2001). An adaptive metropolis algorithm. *Bernoulli*, *7*(2), 223–242. https://doi.org/10.2307/3318737

Hand, M., & Sandiford, M. (1999). Intraplate deformation in central Australia, the link between subsidence and fault reactivation. *Tectonophysics*, *305*(1), 121–140. https://doi.org/10.1016/S0040-1951(99)00009-8

Harris, J. R., Ayer, J., Naghizadeh, M., Smith, R., Snyder, D. B., Behnia, P., et al. (2023). A study of faults in the superior province of Ontario and Quebec using the random forest machine learning algorithm: Spatial relationship to gold mines. *Ore Geology Reviews*, *157*, 105403. https://doi.org/10.1016/j.oregeorev.2023.105403

Hassan, R., Hejrani, B., Medlin, A., Gorbatov, A., & Zhang, F. (2020). High-Performance Seismological tools (HiPerSeis) [Dataset]. *Exploring for the Future: Extended Abstracts*. https://doi.org/10.11636/135095

Haynes, M., Fomin, I., Afonso, J. C., Gorbatov, A., Czarnota, K., & Salajegheh, F. (2020). Developing thermochemical models of Australia's lithosphere. In *Exploring for the future: Extended abstracts* (pp. 1–4). Geoscience Australia. https://doi.org/10.11636/134193

Heaman, L. M., & Kjarsgaard, B. A. (2000). Timing of eastern North American kimberlite magmatism: Continental extension of the great Meteor hotspot track? *Earth and Planetary Science Letters*, *178*(3), 253–268. https://doi.org/10.1016/S0012-821X(00)00079-0

Heaman, L. M., Kjarsgaard, B. A., & Creaser, R. A. (2003). The timing of kimberlite magmatism in North America: Implications for global kimberlite genesis and diamond exploration. *Lithos*, *71*(2), 153–184. https://doi.org/10.1016/j.lithos.2003.07.005

Hejrani, B., Hassan, R., Gorbatov, A., Sambridge, M., Hawkins, R., Valentine, A. P., et al. (2020). Ambient noise tomography of Australia: Application to AusArray deployment [Dataset], *Exploring for the future: Extended abstracts*. In K. Czarnota, I. C. Roach, S. T. Abbott, M. Haynes, N. Kositcin, A. Ray, & E. Slatter (Eds.), (pp. 1–4). Canberra: Geoscience Australia. https://doi.org/10.11636/135130

Hinze, W. J., & Chandler, V. W. (2020). Reviewing the configuration and extent of the Midcontinent rift system. *Precambrian Research*, *342*, 105688. https://doi.org/10.1016/j.precamres.2020.105688

Hoffman, P. (1988). United plates of America, the birth of a craton: Early Proterozoic assembly and growth of Laurentia. *Annual Review of Earth and Planetary Sciences*, *16*(1), 543–603. https://doi.org/10.1146/annurev.ea.16.050188.002551

Hoggard, M. J., Czarnota, K., Richards, F. D., Huston, D. L., Jaques, A. L., & Ghelichkhan, S. (2020). Global distribution of sediment-hosted metals controlled by craton edge stability. *Nature Geoscience*, *13*(7), 504–510. https://doi.org/10.1038/s41561-020-0593-2

Hunt, L., Stachel, T., Grütter, H., Armstrong, J., McCandless, T. E., Simonetti, A., & Tappe, S. (2012). Small mantle fragments from the Renard kimberlites, Quebec: Powerful recorders of mantle lithosphere formation and modification beneath the eastern superior craton. *Journal of Petrology*, *53*(8), 1597–1635. https://doi.org/10.1093/petrology/egs027

Hunter, J. D. (2007). Matplotlib: A 2D graphics environment [Software]. *Computing in Science & Engineering*, *9*(3), 90–95. https://doi.org/10.1109/MCSE.2007.55

Huston, D. L., Champion, D. C., Czarnota, K., Duan, J., Hutchens, M., Paradis, S., et al. (2023). Zinc on the edge—Isotopic and geophysical evidence that cratonic edges control world-class shale-hosted zinc-lead deposits. *Mineralium Deposita*, *58*(4), 707–729. https://doi.org/10.1007/s00126-022-01153-9

Huston, D. L., Doublier, M. P., & Downes, P. M. (2021). *Geological setting, age and endowment of major Australian mineral deposits—A compilation*. (Tech. Rep.). Geoscience Australia. https://doi.org/10.11636/Record.2021.020

Hutchinson, D. R., White, R. S., Cannon, W. F., & Schulz, K. J. (1990). Keweenaw hot spot: Geophysical evidence for a 1.1 Ga mantle plume beneath the midcontinent rift system. *Journal of Geophysical Research*, *95*(B7), 10869–10884. https://doi.org/10.1029/jb095ib07p10869

International Seismological Centre. (2023). ISC-GEM global instrumental earthquake catalogue [Dataset]. https://doi.org/10.31905/d808b825

Ismail-Zadeh, A., Castelli, F., Jones, D., & Sanchez, S. (2023). *Applications of data assimilation and inverse problems in the Earth sciences*. Cambridge University Press.

Jones, A. G., Afonso, J. C., & Fullea, J. (2017). Geochemical and geophysical constrains on the dynamic topography of the Southern African Plateau. *Geochemistry, Geophysics, Geosystems*, *18*(10), 3556–3575. https://doi.org/10.1002/2017GC006908

Kaipio, J., & Somersalo, E. (2005). *Statistical and computational inverse problems*. Springer. https://doi.org/10.1007/b138659

Kaminsky, F., Sablukov, S., Sablukova, L., Shchukin, V., & Canil, D. (2002). Kimberlites from the Wawa area, Ontario. *Canadian Journal of Earth Sciences*, *39*(12), 1819–1838. https://doi.org/10.1139/e02-089

Karato, S.-I., & Karki, B. B. (2001). Origin of lateral variation of seismic wave velocities and density in the deep mantle. *Journal of Geophysical Research*, *106*(B10), 21771–21783. https://doi.org/10.1029/2001JB000214

Kennett, B. L. N., Gorbatov, A., Yuan, H., Agrawal, S., Murdie, R., Doublier, M. P., et al. (2023). Refining the Moho across the Australian continent [Dataset]. *Geophysical Journal International*, *233*(3), 1863–1877. https://doi.org/10.1093/gji/ggad035

Khan, A., & Connolly, J. A. D. (2008). Constraining the composition and thermal state of Mars from inversion of geophysical data. *Journal of Geophysical Research*, *113*(E7). https://doi.org/10.1029/2007JE002996

Kirkby, A., Czarnota, K., Huston, D. L., Champion, D. C., Doublier, M. P., Bedrosian, P. A., et al. (2022). Lithospheric conductors reveal source regions of convergent margin mineral systems. *Scientific Reports*, *12*(1), 8190. https://doi.org/10.1038/s41598-022-11921-2

Klocking, M., Czarnota, K., Champion, D. C., Jaques, A. L., & Davies, D. R. (2020). Spatio-temporal evolution of Australian lithosphere-asthenosphere boundary from mafic volcanism. In K. Czarnota, I. C. Roach, S. T. Abbott, M. Haynes, N. Kositcin, A. Ray, & E. Slatter (Eds.), *Exploring for the future*. Extended abstracts. https://doi.org/10.11636/135075

Koketsu, K., & Sekine, S. (1998). Pseudo-bending method for three-dimensional seismic ray tracing in a spherical Earth with discontinuities. *Geophysical Journal International*, *132*(2), 339–346. https://doi.org/10.1046/j.1365-246x.1998.00427.x

Koohzare, A., Vaníček, P., & Santos, M. (2008). Pattern of recent vertical crustal movements in Canada. *Journal of Geodynamics*, *45*(2–3), 133–145. https://doi.org/10.1016/j.jog.2007.08.001

Korsch, R. J., & Doublier, M. P. (2015). *Major crustal boundaries of Australia* (Tech. Rep.). Geoscience Australia. https://doi.org/10.4225/25/555C181CC0EAE

Kumar, A., Cacace, M., Scheck-Wenderoth, M., Götze, H.-J., & Kaus, B. J. P. (2022). Present-day upper-mantle architecture of the alps: Insights from data-driven dynamic modeling. *Geophysical Research Letters*, *49*(18), e2022GL099476. https://doi.org/10.1029/2022GL099476

Kumar, A., Fernàndez, M., Jiménez-Munt, I., Torne, M., Vergés, J., & Afonso, J. C. (2020). LitMod2D_2.0: An improved integrated geophysical-petrological modeling tool for the physical interpretation of upper mantle anomalies. *Geochemistry, Geophysics, Geosystems*, *21*(3), e2019GC008777. https://doi.org/10.1029/2019GC008777

Kumwenda, J., Betts, P., & Armit, R. (2023). Exposing basement terranes of the North Australian craton. *Earth-Science Reviews*, *237*, 104310. https://doi.org/10.1016/j.earscirev.2022.104310

Kvas, A., Brockmann, J. M., Krauss, S., Schubert, T., Gruber, T., Meyer, U., et al. (2021). GOCO06s – A satellite-only global gravity field model [Dataset]. *Earth System Science Data*, *13*(1), 99–118. https://doi.org/10.5194/essd-13-99-2021

Lawley, C., Kjarsgaard, B. A., Jackson, S., Yang, Z., Petts, D., & Roots, E. (2018). Trace metal and isotopic depth profiles through the Abitibi cratonic mantle. *Lithos*, *314–315*, 520–533. https://doi.org/10.1016/j.lithos.2018.06.026

Leclair, A. D. (2008). Contexte géologique régional du nord-est de la Province du Supérieur. In *Synthèse du Nord-Est de la Province du Supérieur*. [Ministère des ressources naturelles et de la faune], Géologie Québec.

Li, Y., Mascagni, M., & Gorin, A. (2009). A decentralized parallel implementation for parallel tempering algorithm. *Parallel Computing*, *35*(5), 269–283. https://doi.org/10.1016/j.parco.2008.12.009

Ligorria, J., & Ammon, C. (1999). Iterative deconvolution and receiver-function estimation [Software]. *Bulletin of the Seismological Society of America*, *89*(5), 1395–1400. https://doi.org/10.1785/BSSA0890051395

Liu, J. S. (1996). Metropolized independent sampling with comparisons to rejection sampling and importance sampling. *Statistics and Computing*, *6*(2), 113–119. https://doi.org/10.1007/bf00162521

Liu, J. S., Liang, F., & Wong, W. H. (2000). The multiple-try method and local optimization in metropolis sampling. *Journal of the American Statistical Association*, *95*(449), 121–134. https://doi.org/10.2307/2669532

Lu, C., Grand, S. P., Lai, H., & Garnero, E. J. (2019). TX2019slab: A new P and S tomography model incorporating subducting slabs [Dataset]. *Journal of Geophysical Research: Solid Earth*, *124*(11), 11549–11567. https://doi.org/10.1029/2019JB017448

Lyubetskaya, T., & Korenaga, J. (2007). Chemical composition of Earth's primitive mantle and its variance: 1. Method and results. *Journal of Geophysical Research*, *112*(B3), B03212. https://doi.org/10.1029/2005JB004223

Malinverno, A., & Briggs, V. (2004). Expanded uncertainty quantification in inverse problems: Hierarchical Bayes and Empirical Bayes. *Geophysics*, *69*(4), 1005–1016. https://doi.org/10.1190/1.1778243

Malinverno, A., & Parker, R. L. (2006). Two ways to quantify uncertainty in geophysical inverse problems. *Geophysics*, *71*(3), W15–W27. https://doi.org/10.1190/1.2194516

Manassero, M. C., Afonso, J. C., Zyserman, F. I., Jones, A. G., Zlotnik, S., & Fomin, I. (2021). A reduced order approach for probabilistic inversions of 3D Magnetotelluric data II: Joint inversion of MT and surface-wave data. *Journal of Geophysical Research: Solid Earth*, *126*(12), e2021JB021962. https://doi.org/10.1029/2021JB021962

Manassero, M. C., Özaydın, S., Afonso, J. C., Shea, J. J., Ezad, I. S., Kirkby, A., et al. (2024). Lithospheric structure and melting processes in southeast Australia: New constraints from joint probabilistic inversions of 3D magnetotelluric and seismic data. *Journal of Geophysical Research: Solid Earth*, *129*(3), e2023JB028257. https://doi.org/10.1029/2023JB028257

Martinec, Z. (2014). Mass-density Green's functions for the gravitational gradient tensor at different heights [Software]. *Geophysical Journal International*, *196*(3), 1455–1465. https://doi.org/10.1093/gji/ggt495

Martino, L., Elvira, V., Luengo, D., Corander, J., & Louzada, F. (2016). Orthogonal parallel MCMC methods for sampling and optimization. *Digital Signal Processing*, *58*, 64–84. https://doi.org/10.1016/j.dsp.2016.07.013

Martino, L., & Louzada, F. (1997). Issues in the multiple try metropolis mixing. *IEEE Transactions on Evolutionary Computation*, *32*, 239–252. https://doi.org/10.1109/4235.585893

McDonough, W. F., & Sun, S. S. (1995). The composition of the Earth. *Chemical Geology*, *120*(3–4), 223–253. https://doi.org/10.1016/0009-2541(94)00140-4

Meyer, H. O. A., Waldman, M., & Garwood, B. L. (1994). Mantle xenoliths from kimberlite near Kirkland Lake, Ontario. *The Canadian Mineralogist*, *32*, 295–306.

Miles, W. F., & Oneschuk, D. (2016). *Magnetic anomaly map, Canada*. (Tech. Rep.). Geological Survey of Canada. https://doi.org/10.4095/297337

Mints, M. V. (2017). The composite North American craton, superior province: Deep crustal structure and mantle-plume model of Neoarchaean evolution. *Precambrian Research*, *302*, 94–121. https://doi.org/10.1016/j.precamres.2017.08.025

Moorkamp, M. (2017). Integrating electromagnetic data with other geophysical observations for enhanced imaging of the Earth: A tutorial and review. *Surveys in Geophysics*, *38*(5), 935–962. https://doi.org/10.1007/s10712-017-9413-7

Moorkamp, M., Lelièvre, P. G., Linde, N., & Khan, A. (2016). *Integrated imaging of the Earth: Theory and applications*. AGU, American Geophysical Union. Retrieved from https://books.google.com.au/books?id=TD0RkAEACAAJ

Mosegaard, K., & Tarantola, A. (1995). Monte Carlo sampling of solutions to inverse problems. *Journal of Geophysical Research*, *100*(B7), 12431–12447. https://doi.org/10.1029/94JB03097

Musacchio, G., White, D. J., Asudeh, I., & Thomson, C. J. (2004). Lithospheric structure and composition of the Archean Western superior province from seismic refraction/wide-angle reflection and gravity modeling. *Journal of Geophysical Research*, *109*(B3). https://doi.org/10.1029/2003JB002427

Myers, J. S., Shaw, R. D., & Tyler, I. M. (1996). Tectonic evolution of Proterozoic Australia. *Tectonics*, *15*(6), 1431–1446. https://doi.org/10.1029/96TC02356

NOAA. (2022). ETOPO 2022 15 arc-second global relief model [Dataset]. *NOAA National Centers for Environmental Information*. https://doi.org/10.25921/fd45-gt74

Ortega-Gelabert, O., Zlotnik, S., Afonso, J. C., & Díez, P. (2020). Fast stokes flow simulations for geophysical-geodynamic inverse problems and sensitivity analyses based on reduced order modeling. *Journal of Geophysical Research: Solid Earth*, *125*(3), e2019JB018314. https://doi.org/10.1029/2019JB018314

Percival, J. A., Sanborn-Barrie, M., Skulski, T., Stott, G. M., Helmstaedt, H., & White, D. J. (2006). Tectonic evolution of the western superior province from NATMAP and Lithoprobe studies. *Canadian Journal of Earth Sciences*, *43*(7), 1085–1117. https://doi.org/10.1139/e06-062

Percival, J. A., Skulski, T., Sanborn-Barrie, M., Stott, G. M., Leclair, A. D., Corkery, M. T., & Boily, M. (2012). Geology and tectonic evolution of the superior province, Canada. In J. A. Percival, F. A. Cook, & R. M. Clowes (Eds.), *Tectonic styles in Canada: The LITHOPROBE perspective* (Vol. 49, pp. 321–378). Geological Association of Canada.

Perry, H. K. C., Forte, A. M., & Eaton, D. W. S. (2003). Upper-mantle thermochemical structure below North America from seismic-geodynamic flow models. *Geophysical Journal International*, *154*(2), 279–299. https://doi.org/10.1046/j.1365-246X.2003.01961.x

Pilia, S., Davies, D. R., Hall, R., Bacon, C., Gilligan, A., Greenfield, T., et al. (2023). Post-subduction tectonics induced by extension from a lithospheric drip. *Nature Geoscience*, *16*(7), 646–652. https://doi.org/10.1038/s41561-023-01201-7

Pinet, N., Lavoie, D., & Keating, P. (2013). Did the Hudson Strait in Arctic Canada record the opening of the Labrador sea? *Marine and Petroleum Geology*, *48*, 354–365. https://doi.org/10.1016/j.marpetgeo.2013.08.002

Qashqai, T. M., Afonso, J. C., & Yang, Y. (2016). The crustal structure of the Arizona transition zone and southern Colorado Plateau from multiobservable probabilistic inversion. *Geochemistry, Geophysics, Geosystems*, *17*(11), 4308–4332. https://doi.org/10.1002/2016GC006463

Qashqai, T. M., Afonso, J. C., & Yang, Y. (2018). Physical state and structure of the crust beneath the western-central United States from multiobservable probabilistic inversion. *Tectonics*, *37*(9), 3117–3147. https://doi.org/10.1029/2017TC004914

Randall, G. E. (1994). Efficient calculation of complete differential seismograms for laterally homogeneous Earth models. *Geophysical Journal International*, *118*(1), 245–254. https://doi.org/10.1111/j.1365-246x.1994.tb04687.x

Rawlinson, N., Fichtner, A., Sambridge, M., & Young, M. K. (2014). Chapter one—Seismic tomography and the assessment of uncertainty. In R. Dmowska (Ed.), *Advances in geophysics* (Vol. 55, pp. 1–76). Elsevier. https://doi.org/10.1016/bs.agph.2014.08.001

Rawlinson, N., & Sambridge, M. (2005). The fast marching method: An effective tool for tomographic imaging and tracking multiple phases in complex layered media. *Exploration Geophysics*, *36*(4), 341–350. https://doi.org/10.1071/EG05341

Rivers, T. (2015). Tectonic setting and evolution of the Grenville orogen: An assessment of progress over the last 40 years. *Geoscience Canada*, *42*(1), 77–124. https://doi.org/10.12789/geocanj.2014.41.057

Roshanravan, B., Kreuzer, O. P., Bruce, M., Davis, J., & Briggs, M. (2020). Modelling gold potential in the Granites-Tanami orogen, NT, Australia: A comparative study using continuous and data-driven techniques. *Ore Geology Reviews*, *125*, 103661. https://doi.org/10.1016/j.oregeorev.2020.103661

Sage, R. P. (2000). *Kimberlites of the Attawapiskat area, James Bay lowlands, Northern Ontario*. Ontario Geological Survey.

Salters, V. J. M., & Stracke, A. (2004). Composition of the depleted mantle. *Geochemistry, Geophysics, Geosystems*, *5*(5). https://doi.org/10.1029/2003GC000597

Sambridge, M. (2013). A Parallel tempering algorithm for probabilistic sampling and multimodal optimization. *Geophysical Journal International*, *196*(1), 357–374. https://doi.org/10.1093/gji/ggt342

Sambridge, M., & Mosegaard, K. (2002). Monte Carlo methods in geophysical inverse problems. *Reviews of Geophysics*, *40*(3), 3-1–3-29. https://doi.org/10.1029/2000RG000089

Scrimgeour, I. R. (2015). Overview of mineral and petroleum exploration and production in 2014. In *Annual Geoscience Exploration Seminar (AGES) 2015* (pp. 1–16).

Shan, C., Bastani, M., Malehmir, A., Persson, L., & Engdahl, M. (2014). Integrated 2D modeling and interpretation of geophysical and geotechnical data to delineate quick clays at a landslide site in southwest Sweden. *Geophysics*, *79*(4), EN61–EN75. https://doi.org/10.1190/geo2013-0201.1

Simmons, N. A., Forte, A. M., & Grand, S. P. (2009). Joint seismic, geodynamic and mineral physical constraints on three-dimensional mantle heterogeneity: Implications for the relative importance of thermal versus compositional heterogeneity. *Geophysical Journal International*, *177*(3), 1284–1304. https://doi.org/10.1111/j.1365-246X.2009.04133.x

Skirrow, R. G., Wielen, S., Champion, D. C., Czarnota, K., & Thiel, S. (2018). Lithospheric architecture and mantle metasomatism linked to iron oxide Cu–Au ore formation: Multidisciplinary evidence from the Olympic Dam region, South Australia. *Geochemistry, Geophysics, Geosystems*, *19*(8), 2673–2705. https://doi.org/10.1029/2018GC007561

Sleep, N. H. (1990). Monteregian hotspot track: A long-lived mantle plume. *Journal of Geophysical Research*, *95*(B13), 21983–21990. https://doi.org/10.1029/jb095ib13p21983

Smit, K. V., Pearson, D. G., Stachel, T., & Seller, M. (2014). Peridotites from Attawapiskat, Canada: Mesoproterozoic reworking of palaeoarchaean lithospheric mantle beneath the Northern superior superterrane. *Journal of Petrology*, *55*(9), 1829–1863. https://doi.org/10.1093/petrology/egu043

Spencer, S. E. F. (2021). Accelerating adaptation in the adaptive metropolis-Hastings random walk algorithm. *Australian & New Zealand Journal of Statistics*, *63*(3), 468–484. https://doi.org/10.1111/anzs.12344

Stachel, T., Banas, A., Aulbach, S., Smit, K. V., Wescott, P., Chinn, I., et al. (2017). The victor Diamond mine (superior craton, Canada)—A new paradigm for exploration in unconventional settings. In *International Kimberlite Conference: Extended abstracts* (Vol. 11).

Stachel, T., Banas, A., Muehlenbachs, K., Kurszlaukis, S., & Walker, E. (2006). Archean diamonds from Wawa (Canada): Samples from deep cratonic roots predating cratonization of the superior province. *Contributions to Mineralogy and Petrology*, *151*(6), 737–750. https://doi.org/10.1007/s00410-006-0090-7

Stein, C. A., Kley, J., Stein, S., Hindle, D., & Keller, G. R. (2015). North America's Midcontinent rift: When rift met LIP. *Geosphere*, *11*(5), 1607–1616. https://doi.org/10.1130/GES01183.1

Stein, C. A., Stein, S., Merino, M., Keller, G. R., Flesch, L. M., & Jurdy, D. M. (2014). Was the Midcontinent rift part of a successful seafloor-spreading episode? *Geophysical Research Letters*, *41*(5), 1465–1470. https://doi.org/10.1002/2013gl059176

Stewart, A. J., Liu, S. F., Highet, L. M., Woods, M., Czarnota, K., Bonnardot, M., et al. (2020). *Solid Geology of the north Australian craton, 1:1 000 000 scale*. 1st ed (Tech. Rep.). Canberra: Geoscience Australia. https://doi.org/10.26186/135277

Stixrude, L., & Lithgow-Bertelloni, C. (2011). Thermodynamics of mantle minerals—II. Phase equilibria. *Geophysical Journal International*, *184*(3), 1180–1213. https://doi.org/10.1111/j.1365-246X.2010.04890.x

St-Onge, M. R., Searle, M. P., & Wodicka, N. (2006). Trans-Hudson orogen of North America and Himalaya-Karakoram-Tibetan orogen of Asia: Structural and thermal characteristics of the lower and upper plates. *Tectonics*, *25*, TC4006. https://doi.org/10.1029/2005TC001907

St-Onge, M. R., Van Gool, J. A. M., Garde, A. A., & Scott, D. J. (2009). Correlation of Archaean and palaeoproterozoic units between northeastern Canada and western Greenland: Constraining the pre-collisional upper plate accretionary history of the Trans-Hudson orogen. In *Earth accretionary systems in space and time*. Geological Society of London. https://doi.org/10.1144/SP318.7

Stott, G. M., & Corfu, F. (1991). Uchi subprovince. In P. C. Thurston, H. R. Williams, R. H. Sutcliffe, & G. M. Stott (Eds.), *Geology of Ontario* (Vol. 4, pp. 145–238). Ontario Geological Survey. Retrieved from http://www.geologyontario.mndm.gov.on.ca/mndmfiles/pub/data/imaging/SV04-01//SV04-01.pdf

Sudholz, Z. J., Reddicliffe, T. H., Jaques, A. L., Yaxley, G. M., Haynes, M., Gorbatov, A., et al. (2023). Petrology, age, and rift origin of ultramafic lamprophyres (Aillikites) at Mount Webb, a new alkaline province in central Australia. *Geochemistry, Geophysics, Geosystems*, *24*(10), e2023GC011120. https://doi.org/10.1029/2023GC011120

Tarantola, A. (2005). Inverse problem theory and methods for model parameter estimation. *Society for Industrial and Applied Mathematics*. https://doi.org/10.1137/1.9780898717921

Tarantola, A., & Valette, B. (1981). Inverse problems = Quest for information. *Journal of Geophysics*, *50*(1), 159–170. https://doi.org/10.1137/1.9780898717921

Telford, W. M., Geldart, L. P., & Sheriff, R. E. (1990). *Applied geophysics*. Cambridge University Press. Retrieved from https://books.google.com.au/books?id=Q8ogAwAAQBAJ

Tesauro, M., Kaban, M. K., & Aitken, A. R. A. (2020). Thermal and compositional anomalies of the Australian upper mantle from seismic and gravity data. *Geochemistry, Geophysics, Geosystems*, *21*(11), e2020GC009305. https://doi.org/10.1029/2020GC009305

Tesauro, M., Kaban, M. K., Mooney, W. D., & Cloetingh, S. A. P. L. (2014). NACr14: A 3D model for the crustal structure of the North American continent. *Tectonophysics*, *631*, 65–86. https://doi.org/10.1016/j.tecto.2014.04.016

Thompson, D. A., Kendall, J., Helffrich, G. R., Bastow, I. D., Wookey, J., & Snyder, D. B. (2015). CAN-HK: An a priori crustal model for the Canadian shield. *Seismological Research Letters*, *86*(5), 1374–1382. https://doi.org/10.1785/0220150015

Thurston, P. C. (1991). *Geology of Ontario* (Vol. 4). Ontario Ministry of Northern Development and Mines.

Trampert, J., Deschamps, F., Resovsky, J., & Yuen, D. A. (2004). Probabilistic tomography maps chemical heterogeneities throughout the lower mantle. *Science*, *306*(5697), 853–856. https://doi.org/10.1126/science.1101996

Tromp, J. (2020). Seismic wavefield imaging of Earth's interior across scales. *Nature Reviews Earth & Environment*, *1*(1), 40–53. https://doi.org/10.1038/s43017-019-0003-8

Van Rythoven, A., McCandless, T. E., Schulze, D., Bellis, A., Taylor, L., & Liu, Y. (2011). Diamond crystals and their mineral inclusions from the Lynx kimberlite dyke complex, central Quebec. *The Canadian Mineralogist*, *49*(3), 691–706. https://doi.org/10.3749/canmin.49.3.691

Van Staal, C. R., Barr, S. M., & Murphy, J. B. (2012). Provenance and tectonic evolution of Ganderia: Constraints on the evolution of the Iapetus and Rheic oceans. *Geology*, *40*(11), 987–990. https://doi.org/10.1130/G33302.1

Vervaet, F., & Darbyshire, F. A. (2022). Crustal structure around the margins of the eastern superior craton, Canada, from receiver function analysis. *Precambrian Research*, *368*, 106506. https://doi.org/10.1016/j.precamres.2021.106506

Vozar, J., Jones, A. G., Fullea, J., Agius, M. R., Lebedev, S., Le Pape, F., & Wei, W. (2014). Integrated geophysical-petrological modeling of lithosphere-asthenosphere boundary in central Tibet using electromagnetic and seismic data. *Geochemistry, Geophysics, Geosystems*, *15*(10), 3965–3988. https://doi.org/10.1002/2014GC005365

Vrugt, J. A., & Robinson, B. A. (2007). Improved evolutionary optimization from genetically adaptive multimethod search. *Proceedings of the National Academy of Sciences*, *104*(3), 708–711. https://doi.org/10.1073/pnas.0610471104

Walter, M. R., Veevers, J. J., Calver, C. R., & Grey, K. (1995). Neoproterozoic stratigraphy of the centralian superbasin, Australia. *Precambrian Research*, *73*(1), 173–195. https://doi.org/10.1016/0301-9268(94)00077-5

Wessel, P., Luis, J. F., Uieda, L., Scharroo, R., Wobbe, F., Smith, W. H. F., & Tian, D. (2019). The generic mapping tools version 6 [Software]. *Geochemistry, Geophysics, Geosystems*, *20*(11), 5556–5564. https://doi.org/10.1029/2019GC008515

Whitmeyer, S. J., & Karlstrom, K. E. (2007). Tectonic model for the Proterozoic growth of North America. *Geosphere*, *3*(4), 220–259. https://doi.org/10.1130/GES00055.1

Wirth, E. A., Long, M. D., & Moriarty, J. C. (2016). A Markov chain Monte Carlo with gibbs sampling approach to anisotropic receiver function forward modeling. *Geophysical Journal International*, *208*(1), 10–23. https://doi.org/10.1093/gji/ggw383

Wolpert, D. H., & Macready, W. G. (1997). No free lunch theorems for optimization. *IEEE Transactions on Evolutionary Computation*, *1*(1), 67–82. https://doi.org/10.1109/4235.585893

Xu, J., Melgarejo, J. C., Li, Q., Abat, L. T., & Castillo-Oliver, M. (2020). Magma mingling in kimberlites: Evidence from the groundmass cocrystallization of two spinel-group minerals. *Minerals*, *10*(9), 829. https://doi.org/10.3390/min10090829

Yang, X., Li, Y., Afonso, J. C., Yang, Y., & Zhang, A. (2021). Thermochemical state of the upper mantle beneath South China from multi-observable probabilistic inversion. *Journal of Geophysical Research: Solid Earth*, *126*(5), e2020JB021114. https://doi.org/10.1029/2020JB021114

Zhang, A., Afonso, J. C., Xu, Y., Wu, S., Yang, Y., & Yang, B. (2019). The deep lithospheric structure of the Junggar terrane, NW China: Implications for its origin and tectonic evolution. *Journal of Geophysical Research: Solid Earth*, *124*(11), 11615–11638. https://doi.org/10.1029/2019JB018302

Zhang, A., Guo, Z., Afonso, J. C., Shellnutt, J. G., & Yang, Y. (2024). Mantle plume-lithosphere interactions beneath the emeishan large igneous province. *Geophysical Research Letters*, *51*(2), e2023GL106973. https://doi.org/10.1029/2023GL106973

Zhang, A., Guo, Z., Afonso, J. C., Yang, Y., Yang, B., & Xu, Y. (2020). The deep thermochemical structure of the Dabie orogenic belt from multi-observable probabilistic inversion. *Tectonophysics*, *787*, 228478. https://doi.org/10.1016/j.tecto.2020.228478

Zhang, J.-J., Chen, J., Wang, W., Du, Q., & Sun, J. (2023). *Joint inversion and imaging in geophysics*. Frontiers Media SA. Retrieved from https://books.google.com.au/books?id=Ce3VEAAAQBAJ

Zheng, J. P., Lee, C.-T. A., Lu, J. G., Zhao, J. H., Wu, Y. B., Xia, B., et al. (2015). Refertilization-driven destabilization of subcontinental mantle and the importance of initial lithospheric thickness for the fate of continents. *Earth and Planetary Science Letters*, *409*, 225–231. https://doi.org/10.1016/j.epsl.2014.10.042

Zunino, A., Connolly, J. A. D., & Khan, A. (2011). Precalculated phase equilibrium models for geophysical properties of the crust and mantle as a function of composition. *Geochemistry, Geophysics, Geosystems*, *12*(4). https://doi.org/10.1029/2010GC003304

Zurevinski, S. E., Heaman, L. M., Creaser, R. A., & Strand, P. (2008). The churchill kimberlite field, Nunavut, Canada: Petrography, mineral chemistry, and geochronology. *Canadian Journal of Earth Sciences*, *45*(9), 1039–1059. https://doi.org/10.1139/E08-052

Zurevinski, S. E., & Mitchell, R. (2011). Highly evolved hypabyssal kimberlite sills from Wemindji, Quebec, Canada: Insights into the process of flow differentiation in kimberlite magmas. *Contributions to Mineralogy and Petrology*, *161*(5), 765–776. https://doi.org/10.1007/s00410-010-0561-8